Article

Mapping the Dynamics Landscape of Conformational Transitions in Enzyme: The Adenylate Kinase Case

Dechang Li,[1,*] Ming S. Liu,[2,3,*] and Baohua Ji[1,*]
[1]Biomechanics and Biomaterials Laboratory, Department of Applied Mechanics, Beijing Institute of Technology, Beijing, China; [2]CSIRO – Digital Productivity Flagship, Clayton South, Victoria, Australia; and [3]Monash Institute of Medical Research, Clayton, Victoria, Australia

ABSTRACT Conformational transition describes the essential dynamics and mechanism of enzymes in pursuing their various functions. The fundamental and practical challenge to researchers is to quantitatively describe the roles of large-scale dynamic transitions for regulating the catalytic processes. In this study, we tackled this challenge by exploring the pathways and free energy landscape of conformational changes in adenylate kinase (AdK), a key ubiquitous enzyme for cellular energy homeostasis. Using explicit long-timescale (up to microseconds) molecular dynamics and bias-exchange metadynamics simulations, we determined at the atomistic level the intermediate conformational states and mapped the transition pathways of AdK in the presence and absence of ligands. There is clearly chronological operation of the functional domains of AdK. Specifically in the ligand-free AdK, there is no significant energy barrier in the free energy landscape separating the open and closed states. Instead there are multiple intermediate conformational states, which facilitate the rapid transitions of AdK. In the ligand-bound AdK, the closed conformation is energetically most favored with a large energy barrier to open it up, and the conformational population prefers to shift to the closed form coupled with transitions. The results suggest a perspective for a hybrid of conformational selection and induced fit operations of ligand binding to AdK. These observations, depicted in the most comprehensive and quantitative way to date, to our knowledge, emphasize the underlying intrinsic dynamics of AdK and reveal the sophisticated conformational transitions of AdK in fulfilling its enzymatic functions. The developed methodology can also apply to other proteins and biomolecular systems.

INTRODUCTION

Conformational transitions are essential for the function of enzymes (1,2). It is important to understand the relationship between the dynamics of enzyme in conformational transitions and the biological activities (3). For a wide range of enzyme functions, determining the conformational transition pathways and mapping the energy landscape can lead to the design and control of biological processes at the molecular level (4,5). However, this is truly challenging as protein conformational transitions generally span a wide range of timescales and size-scales, and different modes of motion may exhibit complex correlations with various functions. Furthermore, to establish a rational relationship requires multiscale high-resolution dynamics details. A quantitative depiction of the energy landscape and the conformational dynamics at large (~ microsecond timescale or more) is desirable (6,7).

An ideal system for pursuing the dynamics-function rationale is adenylate kinase (AdK) protein, a ubiquitous cellular energy homeostasis enzyme, for catalyzing the phosphoryl transfer between two adenosine diphosphate (ADP) molecules and adenosine triphosphate (ATP) and adenosine monophosphate (AMP), i.e., $Mg^{2+}\cdot ATP + AMP \leftrightarrow Mg^{2+}\cdot ADP + ADP$ (8,9). Structurally AdK consists of two binding sites and three major domains: a CORE domain, an ATP-binding domain (LID), and an AMP-binding domain (NMP), as shown in Fig. 1. AdK can transit between an open conformational state (likely the unbound state) and a closed conformational state (likely with substrates/inhibitors) (8,9). An early experiment (10) showed that the equilibrium state of AdK favors the closed conformation, even in the unbound *apo* state. However, a solution-state NMR experiment (11) showed that binding of ATP induces a dynamic equilibrium of the open and the closed conformations, and the ATP binding motif populates with almost equal populations. Supposedly, for the transition from the open to the closed states, most of the conformational transitions occur at the LID and NMP domains (with the CORE domain being relatively rigid). Henzler-Wildman et al. (2) further showed that the large-scale domain motions in ligand-free AdK are not random, but preferentially follow the pathways capable of proficient chemistry. These experiments show that the enzyme-substrate interactions follow a mechanism different to the conventional induced-fit theories. They suggest a conformational selection/population shift mechanism, where the ligand binding shifts the equilibrium of enzyme's conformational ensembles that preexist regardless of ligands (12–14). However, there remain debates about the

Submitted November 21, 2014, and accepted for publication June 29, 2015.
*Correspondence: dcli@bit.edu.cn or ming.liu@csiro.au or bhji@bit.edu.cn
Editor: Gerhard Hummer

0006-3495/15/08/0647/14
http://dx.doi.org/10.1016/j.bpj.2015.06.059

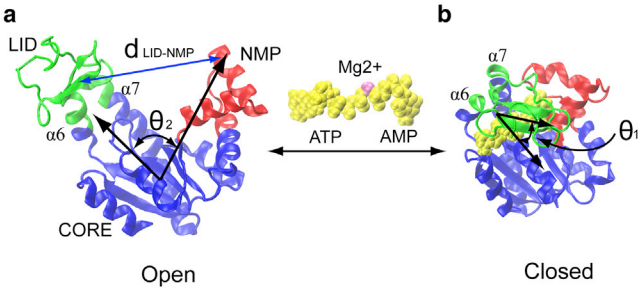

FIGURE 1 Conformational transitions in AdK: (*a*) the open state (e.g., PDB code: 4AKE); and (*b*) the closed state with ligands (e.g., PDB code: 1AKE). The enzyme consists of three well-defined domains: the rigid CORE (*blue*, residues 1–29, 60–121, and 160–214); nucleotide triphosphate binding domain LID (*green*, residues 122–159); and nucleotide monophosphate binding domain NMP (*red*, residues 30–59). The alpha helices $\alpha 6$ and $\alpha 7$ correspond to residues 112 to 122 and residues 160 to 189, respectively. The ligands Mg^{2+}•ATP/AMP are represented by yellow van der Waals (VDW) spheres. The angle LID-CORE θ_1 is formed by the centers of mass of the backbone of residues of LID (a.a. 123–155 (LID), hinge (a.a. 161–165), and CORE (a.a. 1–8, 79–85, 104–110, and 190–198), whereas the angle NMP-CORE θ_2 is formed by the centers of mass of the backbone of residues of NMP (a.a. 50–59), CORE (a.a. 1–8, 79–85, 104–110, and 190–198), and hinge (a.a. 161–165). The variable d_{LN} is used to monitor the distance by the centers of mass between domains LID and NMP, respectively. To see this figure in color, go online.

transition pathways and the conformational selection/population-shift mechanism in AdK (15–21). Consequently a quantitative and molecular understanding of conformational transitions and the energetics of AdK is highly valuable.

A number of theoretical efforts, such as all-atom molecular dynamics (MD) simulations, were done to capture the conformational transitions of AdK with local motions (21–24). However, as demonstrated in experimental works (2), the conformational transitions of AdK are in multitimescale ranging from nanosecond to microsecond and millisecond, which challenges the accessible timescale of all-atom simulations. To overcome the timescale limit and reach the large length scale dynamics of AdK, some coarse-grained models were developed (17–20,25–31) to determine dynamic correlations and transition pathways, and to estimate the free energy changes. Nonetheless, the coarse-grained models lack the atomic details of the interactions, yet the interaction parameters were fitted by all-atom simulations or experimental results. There is still uncertainty and disagreement on the competitive transition orders of the LID and NMP domains and the allostery mechanism in AdK (17,21,22,25–27,29,32,33).

In recent years, to achieve long time simulations using an all-atom description, the accelerating MD simulation methods, such as temperature-enhanced essential dynamics replica exchange (TEE-REX) algorithm (32), have been developed to explore the conformational space of AdK. However, these TEE-REX simulations lack the quantitative description of conformational transitions of AdK. Recently, the umbrella sampling and distance replica exchange methods were applied to calculate the free energy landscape of AdK along its conformational pathways in a one-dimensional reaction coordinate (16,24,34,35). Nonetheless, using a one-dimensional reaction coordinate is insufficient to identify the conformational transitions and pathways of AdK (which typically acts via coupled motion of multidomains). More recently, there have been studies on mapping two-dimensional free energy landscapes of AdK's conformational transition (17,19,27). These two-dimensional free energy landscapes were obtained based on the structure-based coarse-grained model, which lack atomic details of the interactions. Thus to more accurately understand the conformational transitions of AdK, the use of multidimensional free energy landscape with all-atom description is needed.

In this study we aimed to comprehensively understand AdK's operation dynamics and conformational transition mechanism by long timescale (i.e., ~ micro seconds) explicit MD (LT-MD) and bias-exchange metadynamics (BE-META) simulations. BE-META is capable of exhaust sampling of conformational changes and calculating the corresponding free energy landscapes along multidimensional coordinates (36–42). We determined the conformational transitions of *apo* and *ligand*-bound AdKs from the BE-META simulations. Most significantly we quantitatively mapped the free energy landscape of AdK to inclusive transition pathways, which can lead to the design and control of biological processes of AdK at the molecular level. We hope this work helps to advance the knowledge on how conformational transitions affect an enzyme's biological process and functionality.

MATERIALS AND METHODS

We performed long timescale (up to ~ micro seconds) explicit MD and BE-META dynamics simulations of AdK starting from a large variation of states. Table S3 in the Supporting Material summarizes the system MD setups and dynamics and transitions we have observed.

Long-time explicit MD simulations

In LT-MD simulations the starting conformations of AdK were taken from the crystal structures of mesophilic *Escherichia coli* (*E. coli*) deposited in the Protein Data Bank (PDB), i.e., an open state without ligand was adopted from PDB 4AKE (8), and a closed state without ligands was from PDB 1AKE (9) (with the ligand AP_5A removed). For the simulations with ligand, an open state was chosen from PDB 4AKE, in which the ligands ATP and Mg^{2+}•AMP were docked to PDB 4AKE; and a closed state was from PDB 1AKE, in which the ligands ATP and Mg^{2+}•AMP were used instead of AP_5A. Table S3 details the various AdK states we constructed for the MD simulations.

All LT-MD simulations were performed on the GROMACS program (43,44) using the AMBER force field of ffamber03 (45) (with the explicit force field parameters of ATP and AMP by Carlson et al. (46)). The AdK systems were set up following similar procedure of our previous studies (47–49). The protonation states of AdK residues were set normally according to a *pH* 7 environment, e.g., the aspartic residues adopted deprotonation state and the histidine residues were protonated only at its *N*-3 position. The

system was solvated in an approximate $80 \times 80 \times 80$ Å^3 TIP3P (50) water box, with ~15,000 water molecules. Appropriate magnesium ions were added to neutralize the system. Each simulation system contained ~50,000 atoms. The particle mesh Ewald (PME) method (51) was used to calculate the long-range electrostatic interactions. The systems were minimized first using a steepest descent algorithm of 10,000 steps. Then the system was gradually heated to 300 K in 200 ps while positional restraints were used and the restraint force constants were gradually decreased from 2.39 to 0 kcal/(mol·Å^2). All production simulations were fully unrestrained at 300 K with Nose-Hoover (52) thermostat, with a relaxation time of 0.5 ps and a pressure of 1 bar using the Parrinello-Rahman approach (53,54). The LINCS algorithm (55) was applied to constrain the bonds with *H*-atoms. The time step of the production simulations was 2.0 fs. The cutoff of the nonbonded interactions was set to 10 Å. The nonbonded pairs were updated in every 10 steps. Visualization of protein structures was performed using the Visual Molecular Dynamics (VMD) program (56).

The conformational transitions of AdK were monitored by four variables: 1) the root-mean-square deviation (RMSD) of the Cα atoms with reference to the open and closed conformation, 2) the angle of LID-CORE θ_1, 3) the angle of NMP-CORE θ_2, and 4) the distance between LID and NMP d_{LN}, respectively. The two angles θ_1 and θ_2 directly defined the changing state of LID and NMP domain, i.e., in crystal structures, $\theta_1^O \approx 95^\circ$ for LID open (PDB 4AKE) and $\theta_1^C \approx 68^\circ$ for LID closed (PDB 1AKE), $\theta_2^O \approx 61^\circ$ for NMP open (PDB 4AKE) and $\theta_2^C \approx 28^\circ$ for NMP closed (PDB 1AKE) (see Fig. 1). The variable d_{LN} was used to monitor the distance between the center of mass of LID and NMP, e.g., $d_{LN}^O \approx 38$Å in PDB 4AKE and $d_{LN}^C \approx 20$Å in PDB 1AKE, respectively. Table S3 summarizes the distinctive conformational transitions and pathways observed in the LT-MD simulations.

Bias-exchange metadynamics simulations

The BE-META algorithm (36–42) was recently used to accelerate the simulation of rare events and reconstruct the free energy landscape in ligand-receptor binding system (38) and protein folding (36,37). The BE-META technique accelerates rare events by simultaneously biasing several selected reaction coordinates, i.e., the collective variables (CVs). More details of the BE-META algorithm can be found in Text S1 in the Supporting Material and in the works by Laio et al. (36–41). Some of previous studies have chosen various CVs, such as the order parameters in RMSD (10,19,27), the distance between domains (19,35), or the fraction of contacts between different domains (17,34). In this study, we chose CVs of angle LID-CORE θ_1, angle NMP-CORE θ_2 and the distance between LID and NMP d_{LN}, because they are widely used by experimental and structural investigation (which define the open, semi-open–semi-closed, and closed conformations of AdK, see Fig. 1). The parameters implemented in the BE-META simulations were as follows: Gaussian height 0.05 kcal/mol, Gaussian widths 0.01 radian for θ_1 and θ_2, and 0.1 Å for d_{LN}, deposition of a Gaussian every 1 ps, and swaps of bias attempted every 2 ps. To reduce the computational cost and maintain the reasonable conformation of AdK, walls were placed on CVs to restrict them in a reasonable zone: $58^\circ \le \theta_1 \le 100^\circ$, $20^\circ \le \theta_2 \le 70^\circ$, and $15\text{Å} \le d_{LN} \le 45\text{Å}$.

BE-META simulations were performed biasing each of the three CVs on a different replica (plus one replica without any bias) for 200 ns per replica, thus a total of 800 ns timescale per BE-META simulation were conducted in this study, as described in Table S4. It should be noted that the BE-META simulations of free AdK used both the open and closed initial structures, i.e., two replicas started from the open structure (PDB 4AKE) and two started from the closed ones (PDB 1AKE). The different initial structures help sample the open and closed states. Simulations were first equilibrated in NPT ensemble at 300K and 1 bar. After 1 ns of equilibration, the barostat was removed and the BE-META simulation was started. The atomic coordinates were saved every 5 ps and the energy was saved every 0.05 ps. The BE-META simulations were performed in GROMACS (43,44) plus PLUMED package (57), and the results were analyzed using METAGUI (58) developed by Laio and co-workers (36–41) with the VMD program (56).

RESULTS

Conformational transitions and pathways in the ligand-free AdK

We directly observed in LT-MD simulations the large conformational transitions of ligand-free AdK through distinctive pathways, as summarized in Table S3 and illustrated in Figs. 2 and S1–S6.

Simulations starting from the unbound open states show that AdK prefers to shift its conformation from the open to closed state via the following pathways: LID closed first and then NMP moved toward the closed state (see Table S3 and Fig. 2, *a–c*). This pathway is similar to that observed in the TEE-REX MD study (32). Typical trajectories show that the LID domain can be closed from the open state at ~10 ns timescale and reopens on a ~100 ns timescale (see Figs. 2 *a* and S1). Interestingly, from the simulations we observed some intermediate states, where the LID domain is not only close to the CORE domain, but also has contact with the NMP domain while NMP is open (i.e., $\theta_1 \approx 60^\circ \sim 70^\circ$, $\theta_2 \approx 35^\circ \sim 60^\circ$, and $d_{LN} \approx 16\text{Å} \sim 30\text{Å}$; e.g., the snapshots at 300 ns in Fig. 2 *a*, 160 ns in Fig. 2 *b*, and 200 ns in Fig. 2 *c*; also see Figs. S1–S3). These intermediate states deviated from the open crystal structure (e.g., PDB 4AKE) and the closed crystal structure (e.g., PDB 1AKE). Hereafter we referred these intermediate states as the semi-open–semi-closed structures. The intermediate states suggested that the motions of NMP domain can be facilitated by the contact with the LID domain, i.e., the NMP domain moves from the open toward the closed state after the contact established. We showed that the NMP domain can adopt a semi-open state at the timescale of ~100 ns, i.e., with the angle NMP-CORE in the range of $35^\circ \le \theta_2 \le 45^\circ$ (see t = 160 ns in Figs. 2 *b* and S2; the angle is a bit larger than the crystal closed structure $\theta_2^C \approx 28^\circ$). However, given no ligands, no simulation starting from open conformation achieved the crystal closed structure even at the 1,000 ns timescale. This observation is consistent with the NMR experiments (2) showing that the fully closed conformation from the open state occurs on the microsecond-to-millisecond timescale.

Previous unbiased all-atom MD simulations (22,24) showed that AdK stabilizes at the open conformation in ~100 ns timescale when using the CHARMM force field (59,60). In contrast, AdK can transit to the LID closed state in 25~80 ns, a semi-open–semi-close state (23,32), using the OPLS-AA force field (61,62). To compare the results of previous studies, we performed two more LT-MD simulations up to 500 ns timescale starting from the open state using CHARMM (59,60) and OPLS-AA (61,62) force field. As shown in Figs. S11 and S12, AdK is stabilized at the open

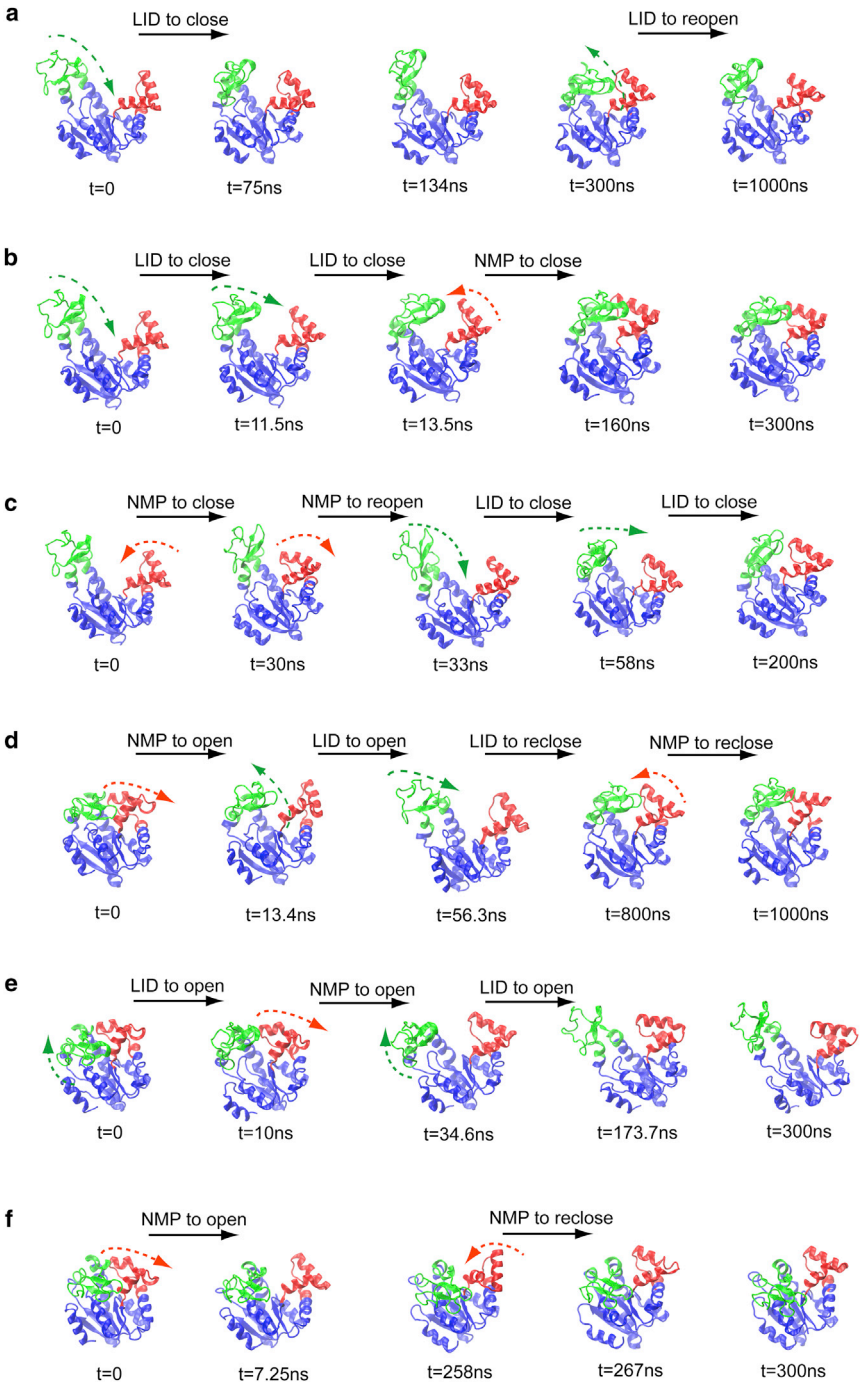

FIGURE 2 Conformational transitions of AdK (without ligands) observed in LT-MD simulations. (*a*) Simulation O_1 starting from the open state, corresponding to the transition: LID open ↔ LID closed. (*b*) Simulation O_2 starting from the open state, corresponding to the transition: 1st step, LID open → LID closed; 2nd step, NMP open → NMP semi-open. (*c*) Simulation O_3 starting from the open state, corresponding to the transition: 1st step, NMP open ↔ NMP semi-open; 2nd step, LID open → LID closed. (*d*) Simulation C_1 starting from the closed state, corresponding to the transition: 1st step, NMP closed ↔ NMP semi-open → NMP open; 2nd step, LID closed ↔ LID open. (*e*) Simulation C_2 starting from the closed state, corresponding to the transition: 1st step, LID closed → LID open; 2nd step, NMP closed → NMP open. (*f*) Simulation C_3 starting from the closed state, corresponding to the transition: NMP closed → NMP semi-open → NMP open → NMP semi-open. More details can be found in Text S2, Table S3, and Figs. S1–S6. To see this figure in color, go online.

state in the 500 ns timescale with the CHARMM27 force field (which is consistent with previous studies (22,24) with the same force field). In contrast, using the OPLS-AA force field, AdK reached the LID closed states within ~100 ns timescale (as shown by t = 169, 250, and 355 ns in Fig. S12), which is similar to the findings in this study and previous ones (23,32). In general, the research community accepts that there is subtle discrepancy when using different force fields (63,64). For example, it was found that Amber force field favors α-helical structures, OPLS-AA overpredicts β-sheet structures, and CHARMM predicts a more stiff transition between the helix and sheet structures (63). This may explain our results that AdK transits from an open to a semi-open–semi-closed state below 100 ns timescale. Our results and conclusions are consistent and coherent under the Amber force field ff03. The comparison of the different force fields, however, is beyond this study.

For the simulations starting from the unbound closed state, we observed two distinct pathways toward the open conformation in independent LT-MD simulations: (I) first,

NMP fluctuated between the closed state and the semi-open state (i.e., $35^\circ \leq \theta_2 \leq 45^\circ$); after the opening of NMP domain, the LID domain then opens gradually (see Table S3 and Figs. 2 *d* and S4); (II) second, LID opens from the closed state rapidly, the NMP domain can stay in the closed state for a couple of nanoseconds before opening (see Table S3 and Figs. 2 *e* and S5). Similar to the simulations starting from the open state, the NMP domain can move toward the semi-open state at the timescale ~100 ns after the closure of LID (see Fig. S4 at t = 800 ns and Fig. S6 at t = 258 ns in Supporting Material). Fig. 2 *f* showed the result that only the NMP domain transits between the closed ↔ semi-open ↔ open conformations, while the LID domain remains in the closed state.

Ligands binding impacts on conformational transitions of AdK

To check the conformational dynamics of AdK when binding with ligands, we docked various ligands into AdK at different states. As found by Åden et al. (65), ATP initiates interactions with the contact surface of CORE when it starts binding. In our simulation, the ligands started docking to the CORE surface around the binding site at the early stage of simulation runs. The simulations starting from the open state bound with ATP and AMP show that the LID domain closes rapidly (while the NMP domain can close to its intermediate state, i.e., $\theta_2 \approx 45^\circ$) much faster than the ligand-free state, with the timescale ~50~100 ns as shown in Figs. 3 *a* and S7. However, even extending the simulation up to 1,000 ns, AdK did not transit to the fully closed conformation (such as PDB 1AKE) (see Figs. 3 *a* and S7). The simulations starting from the open state docked with ATP alone showed identical motions (see Figs. 3 *b* and S8). The simulations with AMP alone led to a more compact structure: the LID domain fully closes and the NMP domain closes to the semi-open state (see Figs. 3 *c* and S9).

When starting from the closed state with both ATP and Mg^{2+}•AMP, the structure is likely stabilized as in the crystal closed conformation (with the angle θ_1 and θ_2 around $\sim 65^\circ$ and $\sim 30^\circ$, respectively (see Figs. 3 *d* and S10). Interestingly, after~125 ns running, the NMP domain presented a significant motion as the NMP-CORE angle θ_2 increased from $\sim 30^\circ$ to $\sim 45^\circ$ in a few nanoseconds. The

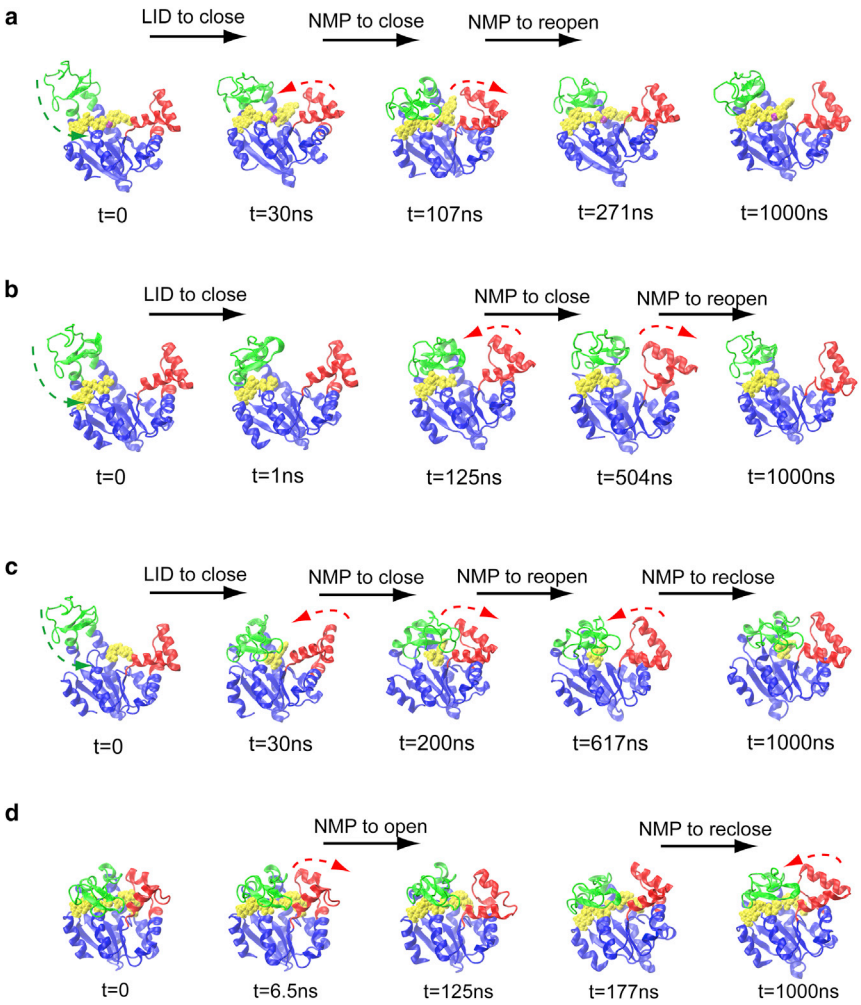

FIGURE 3 Conformational transitions of AdK (with ligands) observed in LT-MD simulations. (*a*) Starting from the open state with both ATP and AMP, simulation O-ATP-AMP. (*b*) Starting from the open state with only ATP, simulation O-ATP. (*c*) Starting from the open state with only AMP, simulation O-AMP. (*d*) Starting from the closed state with both ATP and AMP, simulation C-ATP-AMP. More details can be found in Text S2, Table S3, and Figs. S7–S10. To see this figure in color, go online.

above observation suggests that the LID domain is much more dynamic affinitive than NMP, and the NMP domain motion is the rate-limiting step for enzyme catalysis.

Mapping the transitions and pathways of AdK from LT-MD simulations

Fig. 4 shows the correlations between angles θ_1 and θ_2 during the simulated trajectories, which can quantify the conformational transitions in AdK. LT-MD simulations starting from the open state without ligands, see Fig. 4 *a*, show a significant transition in the angle of LID-CORE, θ_1. Angle θ_1 changes from $\sim 95^\circ$ to$\sim 60^\circ$, corresponding to the open and the closed state of LID domain, respectively. In contrast, the angle of NMP-CORE, θ_2, varies from $\sim 65^\circ$ to $\sim 35^\circ$, corresponding to the open and semi-open state of the NMP domain, respectively (after the LID domain is closed). Fig. 4 *a* shows that the conformation transits as the LID domain closes first and NMP closes afterward. It should be noted that conventional MD simulation suffers insufficient sampling in current timescale, in which intermediate states and conformational transition pathways may miss out. When more independent MD simulations are performed, the complete pathways may be explored (see Fig. S13). For example, AdK also has the probability to follow another pathway that NMP closes first and then LID closes afterward.

Fig. 4 *b* shows the simulations starting from the closed state without ligands have two distinctive conformational transition pathways. The first pathway, indicated by trajectory C_1 and C_3 in Fig. 4 *b* (corresponding to the snapshots of Fig. 2, *d* and *f*, respectively, shows that the NMP domain transits from the closed state to semi-open and to open state, while the LID domain stays in a closed state $(\theta_1 \approx 60^\circ)$. The second pathway, as shown in simulation C_2 in Fig. 4 *b* (corresponding to the snapshots of Fig. 2 *e*), is that LID may open first before NMP opens up. More independent MD simulations starting from the closed state confirmed the existence of these two transition pathways, as shown in Fig. S14.

Significantly, the simulations with bound ligands show different correlations between angles θ_1 and θ_2, as shown in Fig. 4 *c*. From trajectories starting from the closed state (bound with ATP and AMP), a distinct semi-open state of the NMP domain occurs (as indicated by the black dots in Fig. 4 *c*). It shows that AdK now prefers to stay in the close state, yet trajectories starting from the open (bound with ligands) could hardly reach the full close state at the 1,000 ns timescale.

Metadynamics exploration of the free energy landscapes of AdK

Our comprehensive LT-MD simulations show that AdK can undergo dynamic equilibrium between the open and the

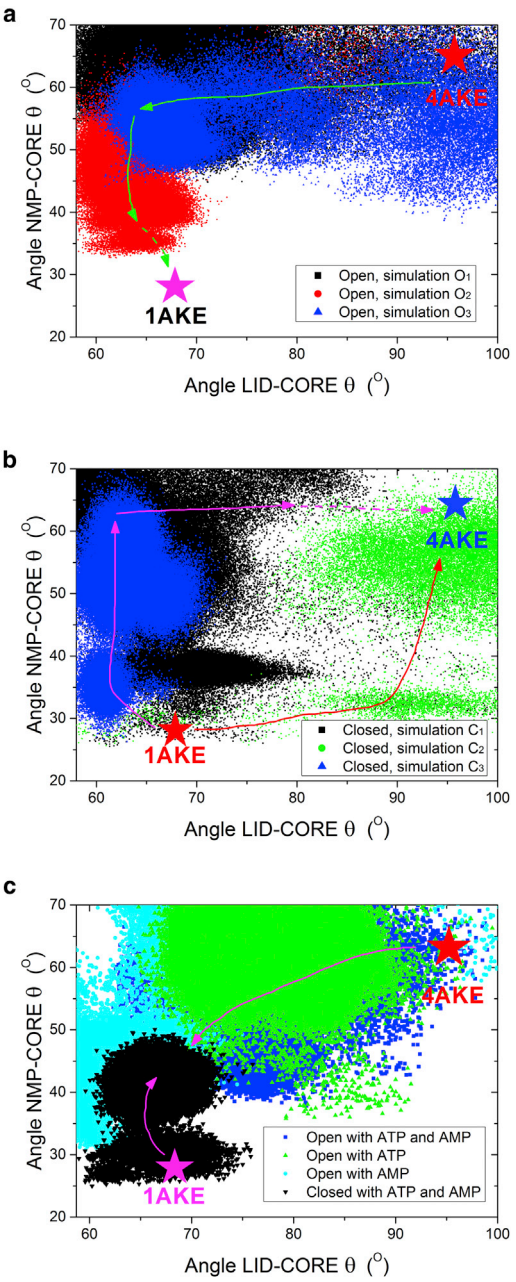

FIGURE 4 The distribution of angles LID-CORE θ_1 and NMP-CORE θ_2 from LT-MD simulations. (*a*) Starting from the open state without ligand, corresponding to simulations O_1, O_2, and O_3. The green line indicates the transition pathway that LID closed first and then NMP to close. (*b*) Starting from the closed state without ligand, corresponding to simulations C_1, C_2, and C_3. The red and pink lines indicate two distinctive transition pathways, one is that NMP open first and then LID to open (*pink line*), and the other one (*red line*) is in the opposite direction. (*c*) Starting from the open or the closed state with ligands, corresponding to simulations O-ATP-AMP, O-ATP, O-AMP, and C-ATP-AMP. The crystal structures of PDB 4AKE and PDB 1AKE are marked. The arrows illustrate the conformational transition and pathways as observed in the LT-MD simulations. (Simulation names can be found in Table S3.) To see this figure in color, go online.

semi-open–semi-closed states (i.e., the LID in closed form and NMP in open or semi-open form) without the presence of ligands, whereas the introduction of ligands shifts the populations of the open and closed forms and to transit AdK into a closed state. According to the LT-MD simulations, AdK follows complex transition pathways and its conformational transitions navigate on a rugged free energy landscapes. However, regular MD simulations suffer from insufficient sampling that some of the conformations are trapped in local energy wells. The LT-MD simulations may miss crucial states and transition pathways. For example, even in our multitrajectory LT-MD simulations up to 1,000 ns timescale, AdK cannot reach the fully closed conformation state from the open state. Hence, mapping these multidimensional landscapes according to specific reaction coordinates is critically important for a molecular and quantitative insight of dynamics and the conformational transition pathways (6). We mapped the energy landscape by BE-META simulations of the AdK system (details as described in Materials and Methods and Tables S3 and S4). The states identified by BE-META simulations along the transition pathways were characterized by three CVs (angle LID-CORE θ_1, angle NMP-CORE θ_2, and the distance between LID and NMP d_{LN}, respectively), as shown in Figs. 5 and 6. Figs. S15 and S16 show that the BE-META simulations converge well while the bias potentials $-V_G^i(S,t)$ are converged to the free energy with corresponding CVs (36). The error on the free energies in metadynamics, estimated according to Marinelli et al. (36), is less than 0.5 kcal/mol. Thus the free energy errors estimated here are ~0.5 kcal/mol.

Metadynamics of the ligand-free AdK

Fig. 5 shows the relative free energy landscape for conformational transitions of the unbound AdK, against two reaction coordinates of angles θ_1 and θ_2. The red line in Fig. 5 indicates the most possible pathway determined by the Metropolis Monte Carlo simulations (with the two end

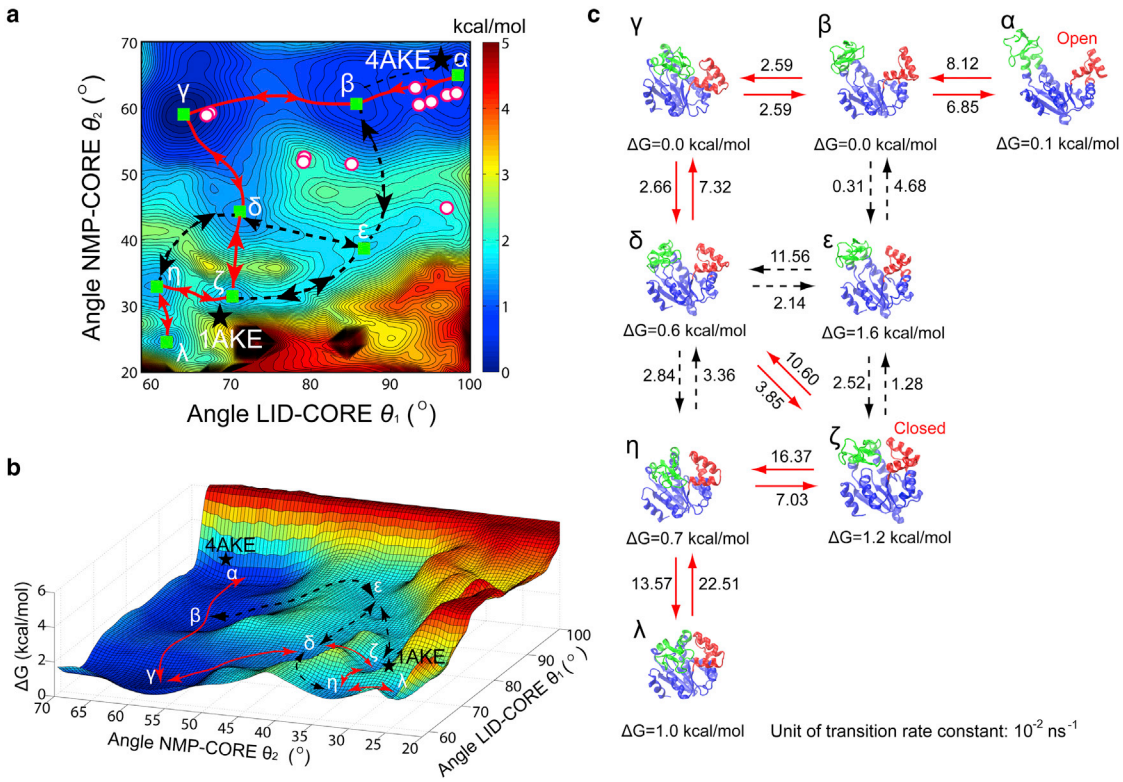

FIGURE 5 BE-META simulations of AdK without ligands. (*a*) A multiwell relative free energy landscape against the CVs of angles LID-CORE θ_1 and NMP-CORE θ_2. The state with the minimum free energy was set as the reference state, i.e., the γ state. The contour map represents the free energy, with the scale bar in kcal/mol units. The states α and ζ correspond to the crystal structures of the open and closed states, respectively.β, γ, δ, and ε indicate the intermediate states corresponding to the semi-open–semi-closed conformations, whereas the states η and λ are more near the closed conformations. The red line indicates the most favorable path. The dashed black lines are possible alternative pathways. The green squares represent the intermediate states. The circular symbols represent the conformational states of AdK crystal structures without ligands (see Table S1). (*b*) A three-dimensional plot of free energy landscapes of the conformational transitions of AdK without ligands. (*c*) Representative conformational transition pathways derived from the free energy landscape. The relative free energy of each state, in kcal/mol (1.0 kcal/mol equal to 1.7 k_BT with temperature 300 K), is labeled below the corresponding structures. The number above the arrows are in 10^{-2} ns^{-1} units, representing the transition rate constants between states as calculated by the Kramers' transition state theory (see Text S3 in the Supporting Material) (88), with the diffusion coefficient $D \approx 4.47 \times 10^{-3} rad^2/ns$ determined from the LT-MD simulations (89,90). To see this figure in color, go online.

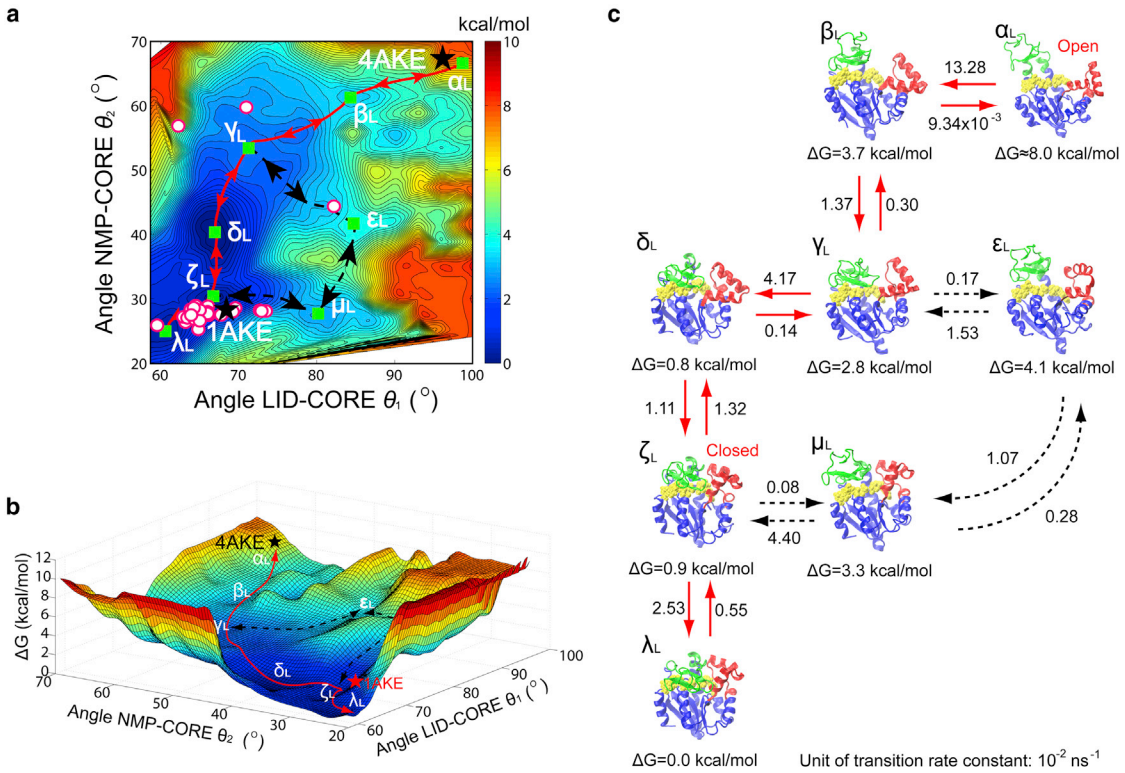

FIGURE 6 BE-META simulations AdK with ligands. (*a*) A multiwell relative free energy landscape with two CVs: angles LID-CORE θ_1 and NMP-CORE θ_2. The state with the minimum free energy was set as the reference state, i.e., the λ_L state. The contour map represents the free energy, with the scale bar in kcal/mol units. The states α_L and ζ_L correspond to the crystal open and closed conformation, respectively. The states β_L, γ_L, δ_L, ε_L and μ_L are the intermediate ones corresponding to the semi-open–semi-closed conformations, whereas the state λ_L is a more compact closed conformation. The red lines indicated the minimum free energy paths. The dashed black lines are the possible alternative pathways. The green squares represent the intermediate states. The circular symbols represent the conformational states of AdK crystal structures with ligands (see Table S2). (*b*) A three-dimensional plot of free energy landscapes of the conformational transitions of AdK with ligands. (*c*) Representative conformational transition pathways derived from the free energy landscape. The relative free energy of each state, in kcal/mol (1.0 kcal/mol equal to 1.7 k_BT with temperature 300 K), is labeled below the corresponding structure. The number above the arrows are in 10^{-2} ns^{-1} units, representing the transition rate constants between the states as calculated by the Kramers' transition state theory (see Text S3 in the Supporting Material) (88), with the diffusion coefficient $D \approx 5.13 \times 10^{-4} rad^2/ns$ determined from the LT-MD simulations (89,90). To see this figure in color, go online.

points set to the open and closed state, respectively). When starting from the open state (e.g., PDB 4AKE), see Fig. 5 *a*, the energy maps indicates that the LID domain should close through the pathway along $\alpha \leftrightarrow \beta \leftrightarrow \gamma$ (reversible in 1,000 ns timescale of LT-MD simulations), as falling in the energy valley (states α, β, and γ are nearly at the same free energy level). We have seen in the BE-META and LT-MD simulations that the conformation is sometimes trapped in intermediate states, where the LID domain closes and is in contact with the NMP domain while the NMP domain stays in the open and/or semi-open state (e.g., the γ and δ configurations, respectively; see also the snapshots at 300 ns in Fig. 2 *a*, 160 ns in Fig. 2 *b*, and 200 ns in Fig. 2 *c* and Figs. S1–S6). After closure of the LID domain, the NMP domain can start closing through the pathway $\gamma \rightarrow \delta \rightarrow \zeta$. This transition pathway needs to climb over a few energy barriers, as shown in Fig. 5. This pathway is consistent with TEE-REX (32) and the structure-based coarse-grained model studies (19,30,31). In comparison with previous works (19,30,31), our current study has more quantitative results with atomistic details. Here we have determined not only the conformational transition pathways, but also the quantitative multidimensional free energy landscape and the critical intermediate states. There is another pathway observed in LT-MD simulations, i.e., NMP closes first and LID closes afterward when starting from open state (see the pathway $\alpha \rightarrow \beta \rightarrow \varepsilon \rightarrow \zeta$, illustrated by the dashed line in Fig. 5).

According to Hammes (66), we calculate the proportion of the two pathways starting from open to closed state, i.e., LID closes first and then NMP closes afterward $(\alpha \rightarrow \beta \rightarrow \gamma \rightarrow \delta \rightarrow \xi)$ and the pathway in which NMP closes first and then LID closes afterward $(\alpha \rightarrow \beta \rightarrow \varepsilon \rightarrow \xi)$

$$\frac{P_{\alpha\rightarrow\beta\rightarrow\gamma\rightarrow\delta\rightarrow\xi}}{P_{\alpha\rightarrow\beta\rightarrow\varepsilon\rightarrow\xi}} = \frac{F_{\alpha\rightarrow\beta\rightarrow\gamma\rightarrow\delta\rightarrow\xi}}{F_{\alpha\rightarrow\beta\rightarrow\varepsilon\rightarrow\xi}} \approx \frac{5.7}{1}, \qquad (1)$$

where $F_{\alpha\rightarrow\beta\rightarrow\gamma\rightarrow\delta\rightarrow\xi}$ and $F_{\alpha\rightarrow\beta\rightarrow\varepsilon\rightarrow\xi}$ are the flux of the conformational transition through the pathway $\alpha \rightarrow \beta \rightarrow \gamma \rightarrow \delta \rightarrow \xi$ and $\alpha \rightarrow \beta \rightarrow \varepsilon \rightarrow \xi$, respectively (see Text S4 in the Supporting Material). This shows that the transition of

AdK mainly follows the pathway in which LID closes first and then NMP closes afterward, which is consistent with Esteban-Martin et al.'s experimental work (67). It also explains our observation in LT-MD simulations that AdK mainly follows this pathway (see Figs. 4, S13, and S14).

The crystal structures show the conformational transition pathway found by BE-META is consistent with the experiments (see the circular symbols in Fig. 5 *a*), that most of the crystal structures of AdK without ligands prefer to the open conformation (i.e., $\theta_1 \approx 95^\circ$ and $\theta_2 \approx 60^\circ$). Specially, there are two crystal structures (i.e., PDB 1AK2 and PDB 2AK2) that stay near the γ state, which confirms the end point of the conformational transition pathway of $\alpha \leftrightarrow \beta \leftrightarrow \gamma$.

Metadynamics of the ligand-bound AdK

The simulations with ligands show significantly different free energy landscape (Fig. 6). The red solid line in Fig. 6 indicates the most-favored transition pathway. There is a clear gorge in the free energy landscape of $\alpha_L \rightarrow \beta_L \rightarrow \gamma_L \rightarrow \delta_L \rightarrow \zeta_L$, corresponding to the conformational transition from the open state to the closed state of AdK. Interestingly, the free energy in the δ_L state (i.e., the semi-open state of NMP) is a bit lower than that in the ζ_L state (i.e., the closed state). Our simulations show the free energy difference between the open and closed state with ligands is about $\Delta G_{O\rightarrow C} \approx 8.0 kcal/mol$ (equal to 13.5 k_BT, corresponding to transition from α_L to ζ_L), which is consistent with previous calculations by Brooks et al. (16). Various points on the transition pathway found by BE-META are consistent with the known crystal structures (see the circular symbols in Fig. 6 *a*). Most of the crystal structures of AdK with ligands stay in the closed state (i.e., $\theta_1 \approx 65^\circ$ and $\theta_2 \approx 28^\circ$). As shown in Fig. 6 *a*, the region around $\theta_1 \approx 90^\circ$ and $\theta_2 \approx 30^\circ$ is energetically strongly unfavorable. This suggests that AdK is unlikely to transit NMP to close first while binding with ligands (also see Fig. 4 *c*). There are two crystal structures found near the γ_L state and one near the ε_L state, which meets the transition pathways found in this study, see Fig. 6 *a*.

DISCUSSION

Rate-limiting step and domain-transition order in AdK

We show that the coordinated conformational transitions over large timescale are intrinsic property of AdK. Compared with previous MD studies at ~100 ns timescale (22–24), our ~1,000 ns LT-MD results have revealed reversible large-scale conformational transitions (i.e., the switch between the open to the semi-open–semi-closed states) of AdK at the 100 ns ~800 ns timescale. LT-MD simulation results indicate that the unbound AdK undergoes rapid dynamic equilibrium between the open and semi-open–semi-closed states, which agree with experimental (10,11) and previous MD studies (22–24). It was proposed that local unfolding and folding, i.e., the cracking, lowers the activation energy barrier for conformational transition of AdK (19,29–31). Cui and coworkers (33) argued that in AdK's transitions the cracking from primary pathways is not necessary. But, as they admitted, local unfolding over short timescale may not reflect the cracking of large conformational transitions. In our LT-MD simulations, we can clearly identify three cracking regions related to the large conformational transitions, i.e., residues 60 to 63, 110 to 120, and 160 to 175, where the secondary structures switched in 10 to 100 ns timescale (see Fig. S17). The three cracking regions found in this study are consistent with previous coarse-grained models (19,29–31). Olsson and Wolf-Watz's experiment suggested that the unfolding and refolding of helixes α6 and α7 (see Fig. 1) is correlated to the closure of the LID domain (68). The cracking regions identified in our study, i.e., residues 110 to 120 and 160 to 175, are exactly the helixes α6 and α7 (see Fig. S17), respectively. Our study also showed that the cracking of helixes α6 and α7 is strongly correlated to the closure of LID domain, which is consistent well with Olsson and Wolf-Watz's experiment (68). This study provides for the first time, to our knowledge, the atomic pictures of the cracking motion and its impacts on the large conformational transition of AdK.

AdK can intrinsically undergo an open to semi-open–semi-closed cycle of conformational changes on the timescale of ~100 ns, but it did not reach a fully closed state at the timescale of a microsecond (when starting from an open structure). Our LT-MD results confirm that the LID domain is much more flexible and affinitive than the NMP domain. Given that, for enzyme, a tight mechanochemical coupling between conformational transitions and chemistry is essential; the motion of NMP domain is the rate-limiting step for AdK's activity.

We have observed that, from the open to the closed state, AdK (in both unbound and ligand-bound states) follows the primary pathway: LID closes first and then in a coordinative fashion NMP closes afterward (see Fig. 5). This observation is consistent with Esteban-Martin et al.'s work (67) in the case of the unbound state. To experimentally verify this order of domain closure, one may do site mutations at helixes α6 and α7 to restrict their cracking motion. It might be observed that the probability of closure of NMP domain decreases because of the restricted opening of LID. In another way, one can design experiments that only allow ATP to bind with LID so that the probability of closure of the NMP domain can be increased because the ATP-induced closure of LID facilitates the closing of NMP.

Ligand-binding can induce a population-shift mechanism

Our LT-MD simulations showed that AdK can transform (at a timescale of ~100 ns) from the open to the semi-open–

semi-closed state reversibly even without ligands; this agrees well with the experiment results (2,10,11) that the transition between the open and the closed states of AdK undergo dynamic equilibrium in the absence of ligands. The simulations with ligands showed a more compact structure because of the interactions with ligands. This is consistent with the experiments (2,10,11) that the presence of ligands shifts the populations of the open/closed states and changes the transition rates.

We observed that the open state of AdK can quickly reach a few semi-open–semi-closed states (see in Fig. 5 *a* the open circles around states γ and δ, such as PDB 1AK2 and PDB 2AK2). Fig. 5 indicates that AdK conformation favors the open state without ligands, as observed from many crystal structures (8,9). Single-molecular FRET experiment by Henzler-Wildman et al. (2) also showed that the open state is a major population in the absence of ligand. However, another FRET experiment by Hanson et al. (10) suggested that the equilibrated conformation of AdK favors the closed state in the absence of ligands. We understand that, the two FRET experiments have different labeling positions, i.e., in the FRET experiment by Henzler-Wildman et al. (2), the dyes were tagged to residues Lys145 and Ile52 (which are located at the LID and NMP domains, respectively), whereas in the experiment by Hanson et al. (10), the dyes were tagged to residues Ala127 and Ala194 (which are located at the LID and CORE domains, respectively). Therefore, Henzler-Wildman et al.'s experiment (2), measuring the motion of LID and NMP domains, showed the open state (corresponding to α or β states) was more favorable; but the experiments by Hanson et al.'s (10), measuring the motion of LID domain alone, showed the close state (corresponding to γ state) was more favorable.

Fig. 7 shows the distribution of the distance $\boldsymbol{d}_{\mathrm{LN}}$ and $\boldsymbol{d}_{\mathbf{LC}}$, which are corresponding to the distance between the dyes in FRET experiment by Henzler-Wildman et al. (2) and Hanson et al. (10), respectively. Provided with no ligand, the LID-NMP $\boldsymbol{d}_{\mathrm{LN}}$ distribution significantly showed two major states, i.e., with and without LID-NMP contact. This result is consistent with the finding of Henzler-Wildman et al.'s FRET experiment (2). That is, both of the two states sampled to significant fractions even in the absence of any ligand, in which the fraction of closed-like state is smaller than that of open-like state. While binding with ligands, the enzyme is confined to the closed state with a more compact structure. However, when the dyes label changed to the LID and CORE domains (i.e., in Hanson et al.'s FRET experiment (10)), the LID-CORE $\boldsymbol{d}_{\mathbf{LC}}$ with a bias-weighted preference for LID was closed to the CORE domain (see Fig. 7 *b*). Obviously, the AdK in these states could still be in the open form because of the opening of the NMP domain. Once bound with ligands, $\boldsymbol{d}_{\mathbf{LC}}$ is confined to the closed state with a more compact structure. The above results demonstrate the population shift mechanism. It also solves the puzzle raised by the different results in the above two single-molecular FRET experiments (2,10), which is caused by the different labeling position. Our simulation results show that in the intermediate states (e.g., states β, γ, and δ in Fig. 5) LID closes to contact with NMP/CORE and causes the decreasing of the distance $\boldsymbol{d}_{\mathrm{LN}}$ and $\boldsymbol{d}_{\mathbf{LC}}$. Consequently, the closed state indicated by FRET experiment is likely a semi-open–semi-closed conformation, but not the fully closed state of the AdK's LID and NMP domains. As argued by Potoyan et al. (34), the conformation state of AdK near the open state may still retain many LID-NMP contacts, suggesting that the free energy basin of the closed state is larger than expected. Our BE-META dynamics results show that AdK has this type of free energy landscape, e.g., in Fig. 5 *a*, the γ and δ states correspond to the intermediate states that the LID domain has contacts with NMP while NMP is open or semi-open. Now we prove that there is a discrepancy in the relative populations of the

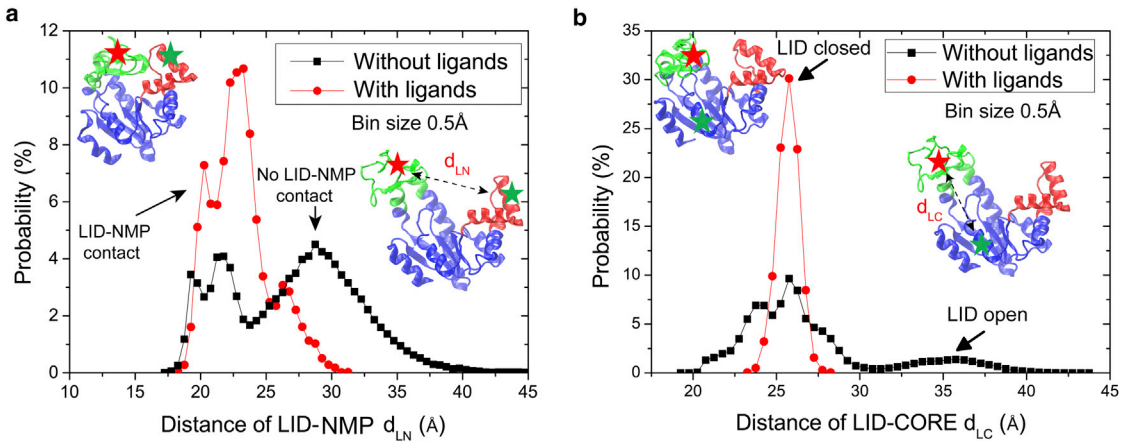

FIGURE 7 The distribution of distance (*a*) $\boldsymbol{d}_{\mathrm{LN}}$ between the LID and NMP domains and (*b*) $\boldsymbol{d}_{\mathrm{LC}}$ between the LID and CORE domains based on LT-MD simulations. The insets illustrate the corresponding conformations. The stars illustrate the labeling positions in single-molecule FRET experiments. The bin size of the distance is 0.5 Å. To see this figure in color, go online.

open and closed state of the unbound AdK, as observed in FRET experiments (2,10) as well as predicted by other simulations (34).

Intermediate states critical for the conformational transitions

Recently, Esteban-Martin et al. (67) exploited the shape information encoded in residual dipolar couplings via steric alignment by NMR. They found experimental evidence that there is a closed-like state in the absence of substrate with high probability along the opening/closing pathway of AdK. From the LT-MD simulations, we observed a few intermediate conformational states: the LID domain is closing to the CORE domain and has contact with the NMP domain, while NMP is in open/semi-open states (such as the snapshots at 300 ns in Fig. 2 *a*, 160 ns in Fig. 2 *b*, and 200 ns in Fig. 2 *c*; see also Figs. S1–S3). These intermediate states are also exclusively identified in the BE-META simulations, e.g., the γ and δ states in landscape of Fig. 5 and the γ_L and δ_L states in Fig. 6 (also see Fig. S18). These intermediate conformations suggest the existence of the closed-like state along the transition pathway, as identified by Esteban-Martin et al. (67), and by the crystal structures of PDB 1AK2 and PDB 2AK2 around γ state (see Fig. 5 *a* and Table S1), and PDB 1DVR and PDB 2C9Y around γ_L state (see Fig. 6 *a* and Table S2).

Dynamically these intermediate states are the key steps of motion of the NMP domain, i.e., the NMP domain moves from the open toward the closed state after forming the contact with the LID domain. We conclude that transiting through the key intermediate states is critical for AdK's operating mechanism. These intermediates tell us not only the domains' transition order, but also the stepwise paths how NMP motion is rate-limiting and how two binding sites cooperate with each other.

Multiwell free energy landscape allows conformational selection and induced fit operations coupling the conformational transitions

A few previous studies (16,24,34,35) have constructed one-dimensional free energy landscape of AdK's dynamic changes. However, the one-dimensional reaction coordinate is insufficient to capture the conformational changes of AdK, where multidomain motions and two binding site activation are coupled. For example, as shown in the insets of Fig. S18, a one-dimensional free energy landscape against the distance of LID-NMP $\boldsymbol{d_{LN}}$ does indicate the double-well pattern and shifted population upon ligand binding (collectively averaging all possible states regardless the collective variables of $\boldsymbol{\theta_1}$, and $\boldsymbol{\theta_2}$). But once we construct the multidimensional free energy landscape by simultaneously searching and mapping the dynamic angles $\boldsymbol{\theta_1}$, and $\boldsymbol{\theta_2}$ and distance between LID, CORE, and NMP (i.e., the distance $\boldsymbol{d_{LN}}$ is well related to the single-molecular FRET experiment (10)), the three-dimensional free-energy landscapes showed more complex but complete conformational transition pathways (see Fig. S18), in comparison with the one- and two-dimensional landscapes (i.e., Figs. 5 and 6).

Our simulation of AdK without ligands indicates that the open $\leftrightarrow$ closed free energy difference is only a few kcal/mol (in the range of 1~2 k_BT, which agrees with previous estimations (16,24,34,35)). Most significantly, the free energy landscape found from our study is in a good quantitative agreement with the single-molecular FRET and NMR spin relaxation experiments (which reported fast collective domain motions that take place on a nanosecond timescale). A relatively rare event of attaining catalytically competent closed conformation (e.g., consistent with x-ray structure for the closed state) on a microsecond timescale is also captured (2,69). From the biological perspective, the relatively small free energy difference between conformations can facilitate fine control of transitions by environmental perturbations and signaling (34). The low-barrier free energy landscape of ligand-free AdK suggests that the transitions between the open and the closed states of AdK can undergo dynamic equilibrium even without the induction of ligand, as known from some experiments (10,11). Even in the intermediate states in which LID-NMP form contacts that last for a long timescale, the typical conformations are still structurally similar to the open state. These suggest a transition state for domain opening (see Fig. S1) or domain closing (see Fig. S2) may occur.

Furthermore, the free energy landscape shows us that open-like conformations are heavily populated and transit to the closed states in the presence of ligands (see Figs. 5, 6, and 7, strongly indicating that the conformational population shifted by the interaction with ligands). There is no clear minimum toward the ligand-bound open state (see the α_L state in Fig. 6 *a*), indicating that the ligand does not bind effectively to a fully open conformation of AdK, but somewhere later along the pathway. This mechanism was also predicted by Arora and Brooks (16). It was suggested that the multiwell free energy landscape of free enzyme supports a conformational selection/population shift operation (70). However, it was proposed that enzymes with LID-gated active sites should operate by an induced fit mechanism instead of conformational selection (70). Although AdK has a multiwell energy landscape and the closed conformation preexists, the fully closed state of AdK cannot capture the ligands because the closure of LID/NMP prevents ligands from binding to their active sites. Hammes et al. (66) proposed that both of the conformational selection and induced fit operations may occur, depending on the ligand and protein concentrations. As shown in Fig. 5, there are a few of intermediate states that the LID/NMP domains are in semi-open–semi-closed conformations (such as the β, γ, δ, and ε states in Fig. 5).

The semi-open–semi-closed intermediate states do not rule out the binding of ligands with these states. Once the ligand binds to these accessible intermediate states, it should change the shape of the free energy landscape of AdK toward the fully closed conformations. Consequently, mechanism of ligand binding to AdK could involve both conformational selection and induced fit operations. When the ligand is in low concentration, the conformational selection will dominate, because the binding of ligand is in low stochastic frequency compared with the conformational transition of protein. In contrast, the mechanism will switch to be dominated by induced fit at high ligand concentration (66). Accordingly, our findings suggest a plausible perspective for a hybrid of conformational selection and induced fit operations of ligand binding to AdK. This mechanism was once suggested by Åden et al. (65) for the binding of ATP to AdK. It was also found in other systems, e.g., the dihydrofolate reductase and flavodoxin (66).

CONCLUSIONS

We applied extensive long timescale explicit MD and BE-META simulations to explore the pathways and free energy landscape of dynamic changes in AdK. We have comprehensively determined at atomistic level the transition pathways and intermediate states of AdK in the presence and absence of ligands; most significantly, we quantitatively mapped the free energy landscape of AdK to its dynamic transitions. In AdK, there is chronological operation of the functional domains. Specifically the free energy landscape reveals that in the ligand-free state, we identified the low-energy barriers to intermediate conformational states that facilitate the transitions of AdK by environmental perturbations and signaling. Once bound with a ligand, the conformational population of AdK prefers to shift to the closed form. These observations help to establish insightful pictures of intrinsic dynamics of AdK, and rationalize the complex conformational transitions of AdK in regulating its enzymatic functions. We have suggested a perspective for a hybrid of conformational selection and induced fit operations of ligand binding to AdK. This methodology can also extend to apply on other enzymes and biomolecular systems.

For understanding the regulation in protein functions, researchers have been bypassing the static structures interpretation and focusing more on dynamics, flexibility, and fluctuations (14). We show in this article AdK functionalities are accomplished via, to our knowledge, novel dynamics (e.g., a hybrid of conformational selection and induced fit operations). This suggests that a dynamics-based strategy to investigate the design of proteins and ligands systems is critically important. It is increasingly accepted that conformational couplings are intrinsic properties for all proteins in action (71). A rational design of ligands targeting the population shift, conformational transitions, fluctuations, and flexibility of protein (17,72) shall be core practice for development of enzymes and other biomolecular systems.

SUPPORTING MATERIAL

Supporting Materials and Methods, 18 figures, and four tables are available at http://www.biophysj.org/biophysj/supplemental/S0006-3495(15)00617-7.

AUTHOR CONTRIBUTIONS

D.C.L., M.S.L., and B.H.J. conceived and designed the research; D.C.L. and M.S.L. performed the experiments; D.C.L., M.S.L., and B.H.J. analyzed the data; and D.C.L., M.S.L., and B.H.J. wrote the article.

ACKNOWLEDGMENTS

We thank the support from the National Science Foundation of China (Grant Nos. 11025208, 11221202, 11372042, and 11202026). M.S.L. acknowledges the support from CSIRO - Computational and Simulation Sciences TCP, CAFHS' Capability Development Fund, and CSIRO - Advanced Materials TCP. The authors also thank the generous allocation of computing merits by Australian NCI supercomputers.

SUPPORTING CITATIONS

References (73–87) appear in the Supporting Material.

REFERENCES

1. Kern, D., and E. R. P. Zuiderweg. 2003. The role of dynamics in allosteric regulation. *Curr. Opin. Struct. Biol.* 13:748–757.
2. Henzler-Wildman, K. A., V. Thai, …, D. Kern. 2007. Intrinsic motions along an enzymatic reaction trajectory. *Nature.* 450:838–844.
3. Tsai, C.-J., A. del Sol, and R. Nussinov. 2008. Allostery: absence of a change in shape does not imply that allostery is not at play. *J. Mol. Biol.* 378:1–11.
4. Lee, G. M., and C. S. Craik. 2009. Trapping moving targets with small molecules. *Science.* 324:213–215.
5. Smock, R. G., and L. M. Gierasch. 2009. Sending signals dynamically. *Science.* 324:198–203.
6. Tsai, C.-J., and R. Nussinov. 2014. A unified view of "how allostery works.". *PLOS Comput. Biol.* 10:e1003394.
7. Cornish-Bowden, A. 2014. Understanding allosteric and cooperative interactions in enzymes. *FEBS J.* 281:621–632.
8. Müller, C. W., G. J. Schlauderer, …, G. E. Schulz. 1996. Adenylate kinase motions during catalysis: an energetic counterweight balancing substrate binding. *Structure.* 4:147–156.
9. Müller, C. W., and G. E. Schulz. 1992. Structure of the complex between adenylate kinase from Escherichia coli and the inhibitor Ap5A refined at 1.9 A resolution. A model for a catalytic transition state. *J. Mol. Biol.* 224:159–177.
10. Hanson, J. A., K. Duderstadt, …, H. Yang. 2007. Illuminating the mechanistic roles of enzyme conformational dynamics. *Proc. Natl. Acad. Sci. USA.* 104:18055–18060.
11. Adén, J., and M. Wolf-Watz. 2007. NMR identification of transient complexes critical to adenylate kinase catalysis. *J. Am. Chem. Soc.* 129:14003–14012.
12. Koshland, D. E. 1958. Application of a theory of enzyme specificity to protein synthesis. *Proc. Natl. Acad. Sci. USA.* 44:98–104.

13. Koshland, Jr., D. E. 1994. The key-lock theory and the induced fit theory. *Angew. Chem. Int.* 33:2375–2378.
14. Laskowski, R. A., F. Gerick, and J. M. Thornton. 2009. The structural basis of allosteric regulation in proteins. *FEBS Lett.* 583:1692–1698.
15. Ådén, J., A. Verma, …, M. Wolf-Watz. 2012. Modulation of a pre-existing conformational equilibrium tunes adenylate kinase activity. *J. Am. Chem. Soc.* 134:16562–16570.
16. Arora, K., and C. L. Brooks, 3rd. 2007. Large-scale allosteric conformational transitions of adenylate kinase appear to involve a population-shift mechanism. *Proc. Natl. Acad. Sci. USA.* 104:18496–18501.
17. Wang, Y., L. Gan, …, J. Wang. 2013. Exploring the dynamic functional landscape of adenylate kinase modulated by substrates. *J. Chem. Theory Comput.* 9:84–95.
18. Liu, M. S., B. D. Todd, and R. J. Sadus. 2010. Allosteric conformational transition in adenylate kinase: dynamic correlations and implication for allostery. *Aust. J. Chem.* 63:405–412.
19. Whitford, P. C., O. Miyashita, …, J. N. Onuchic. 2007. Conformational transitions of adenylate kinase: switching by cracking. *J. Mol. Biol.* 366:1661–1671.
20. Daily, M. D., L. Makowski, …, Q. Cui. 2012. Large-scale motions in the adenylate kinase solution ensemble: coarse-grained simulations and comparison with solution x-ray scattering. *Chem. Phys.* 396:84–91.
21. Beckstein, O., E. J. Denning, …, T. B. Woolf. 2009. Zipping and unzipping of adenylate kinase: atomistic insights into the ensemble of open<–>closed transitions. *J. Mol. Biol.* 394:160–176.
22. Brokaw, J. B., and J.-W. Chu. 2010. On the roles of substrate binding and hinge unfolding in conformational changes of adenylate kinase. *Biophys. J.* 99:3420–3429.
23. Pontiggia, F., A. Zen, and C. Micheletti. 2008. Small- and large-scale conformational changes of adenylate kinase: a molecular dynamics study of the subdomain motion and mechanics. *Biophys. J.* 95:5901–5912.
24. Song, H. D., and F. Zhu. 2013. Conformational dynamics of a ligand-free adenylate kinase. *PLoS One.* 8:e68023.
25. Daily, M. D., G. N. Phillips, Jr., and Q. Cui. 2010. Many local motions cooperate to produce the adenylate kinase conformational transition. *J. Mol. Biol.* 400:618–631.
26. Chu, J.-W., and G. A. Voth. 2007. Coarse-grained free energy functions for studying protein conformational changes: a double-well network model. *Biophys. J.* 93:3860–3871.
27. Lu, Q., and J. Wang. 2008. Single molecule conformational dynamics of adenylate kinase: energy landscape, structural correlations, and transition state ensembles. *J. Am. Chem. Soc.* 130:4772–4783.
28. Korkut, A., and W. A. Hendrickson. 2009. Computation of conformational transitions in proteins by virtual atom molecular mechanics as validated in application to adenylate kinase. *Proc. Natl. Acad. Sci. USA.* 106:15673–15678.
29. Maragakis, P., and M. Karplus. 2005. Large amplitude conformational change in proteins explored with a plastic network model: adenylate kinase. *J. Mol. Biol.* 352:807–822.
30. Miyashita, O., J. N. Onuchic, and P. G. Wolynes. 2003. Nonlinear elasticity, proteinquakes, and the energy landscapes of functional transitions in proteins. *Proc. Natl. Acad. Sci. USA.* 100:12570–12575.
31. Miyashita, O., P. G. Wolynes, and J. N. Onuchic. 2005. Simple energy landscape model for the kinetics of functional transitions in proteins. *J. Phys. Chem. B.* 109:1959–1969.
32. Kubitzki, M. B., and B. L. de Groot. 2008. The atomistic mechanism of conformational transition in adenylate kinase: a TEE-REX molecular dynamics study. *Structure.* 16:1175–1182.
33. Daily, M. D., H. Yu, …, Q. Cui. 2013. Allosteric activation transitions in enzymes and biomolecular motors: insights from atomistic and coarse-grained simulations. *In* Dynamics in Enzyme Catalysis. Springer, Heidelberg, Berlin, pp. 139–164.
34. Potoyan, D. A., P. I. Zhuravlev, and G. A. Papoian. 2012. Computing free energy of a large-scale allosteric transition in adenylate kinase using all atom explicit solvent simulations. *J. Phys. Chem. B.* 116:1709–1715.
35. Lou, H., and R. I. Cukier. 2006. Molecular dynamics of apo-adenylate kinase: a distance replica exchange method for the free energy of conformational fluctuations. *J. Phys. Chem. B.* 110:24121–24137.
36. Marinelli, F., F. Pietrucci, …, S. Piana. 2009. A kinetic model of trp-cage folding from multiple biased molecular dynamics simulations. *PLOS Comput. Biol.* 5:e1000452.
37. Piana, S., and A. Laio. 2007. A bias-exchange approach to protein folding. *J. Phys. Chem. B.* 111:4553–4559.
38. Pietrucci, F., F. Marinelli, …, A. Laio. 2009. Substrate binding mechanism of HIV-1 protease from explicit-solvent atomistic simulations. *J. Am. Chem. Soc.* 131:11811–11818.
39. Laio, A., and F. L. Gervasio. 2008. Metadynamics: a method to simulate rare events and reconstruct the free energy in biophysics, chemistry and material science. *Rep. Prog. Phys.* 71:126601.
40. Barducci, A., G. Bussi, and M. Parrinello. 2008. Well-tempered metadynamics: a smoothly converging and tunable free-energy method. *Phys. Rev. Lett.* 100:020603.
41. Laio, A., and M. Parrinello. 2002. Escaping free-energy minima. *Proc. Natl. Acad. Sci. USA.* 99:12562–12566.
42. Okazaki, K., and G. Hummer. 2013. Phosphate release coupled to rotary motion of F1-ATPase. *Proc. Natl. Acad. Sci. USA.* 110:16468–16473.
43. Berendsen, H. J. C., D. Van der Spoel, and R. Vandrunen. 1995. Gromacs: a message-passing parallel molecular dynamics implementation. *Comput. Phys. Commun.* 91:43–56.
44. Lindahl, E., B. Hess, and D. van der Spoel. 2001. GROMACS 3.0: a package for molecular simulation and trajectory analysis. *J. Mol. Model.* 7:306–317.
45. Duan, Y., C. Wu, …, P. Kollman. 2003. A point-charge force field for molecular mechanics simulations of proteins based on condensed-phase quantum mechanical calculations. *J. Comput. Chem.* 24:1999–2012.
46. Meagher, K. L., L. T. Redman, and H. A. Carlson. 2003. Development of polyphosphate parameters for use with the AMBER force field. *J. Comput. Chem.* 24:1016–1025.
47. Li, D., B. Ji, …, Y. Huang. 2011. Strength of hydrogen bond network takes crucial roles in the dissociation process of inhibitors from the HIV-1 protease binding pocket. *PLoS One.* 6:e19268.
48. Li, D., B. Ji, …, Y. Huang. 2010. Crucial roles of the subnanosecond local dynamics of the flap tips in the global conformational changes of HIV-1 protease. *J. Phys. Chem. B.* 114:3060–3069.
49. Li, D.-C., and B.-H. Ji. 2012. Free energy calculation of single molecular interaction using Jarzynski's identity method: the case of HIV-1 protease inhibitor system. *Acta Mech. Sin.* 28:891–903.
50. Jorgensen, W. L., J. Chandrasekhar, …, M. L. Klein. 1983. Comparison of simple potential functions for simulating liquid water. *J. Chem. Phys.* 79:926–935.
51. Essmann, U., L. Perera, …, L. G. Pedersen. 1995. A smooth particle mesh Ewald method. *J. Chem. Phys.* 103:8577–8593.
52. Nose, S. 1984. A molecular dynamics method for simulations in the canonical ensemble. *Mol. Phys.* 52:255–268.
53. Parrinello, M., and A. Rahman. 1981. Polymorphic transitions in single crystals: a new molecular dynamics method. *J. Appl. Phys.* 52:7182.
54. Nose, S., and M. L. Klein. 1983. Constant pressure molecular dynamics for molecular systems. *Mol. Phys.* 50:1055–1076.
55. Hess, B. 2008. P-LINCS: a parallel linear constraint solver for molecular simulation. *J. Chem. Theory Comput.* 4:116–122.
56. Humphrey, W., A. Dalke, and K. Schulten. 1996. VMD: visual molecular dynamics. *J. Mol. Graph.* 14:33–38.
57. Bonomi, M., D. Branduardi, …, M. Parrinello. 2009. PLUMED: a portable plugin for free-energy calculations with molecular dynamics. *Comput. Phys. Commun.* 180:1961–1972.

58. Biarnés, X., F. Pietrucci, …, A. Laio. 2012. METAGUI. A VMD interface for analyzing metadynamics and molecular dynamics simulations. *Comput. Phys. Commun.* 183:203–211.

59. MacKerell, A. D., D. Bashford, …, M. Karplus. 1998. All-atom empirical potential for molecular modeling and dynamics studies of proteins. *J. Phys. Chem. B.* 102:3586–3616.

60. MacKerell, Jr., A. D., M. Feig, and C. L. Brooks, 3rd. 2004. Improved treatment of the protein backbone in empirical force fields. *J. Am. Chem. Soc.* 126:698–699.

61. Kaminski, G. A., R. A. Friesner, …, W. L. Jorgensen. 2001. Evaluation and reparametrization of the OPLS-AA force field for proteins via comparison with accurate quantum chemical calculations on peptides. *J. Phys. Chem. B.* 105:6474–6487.

62. Jorgensen, W. L., D. S. Maxwell, and J. Tirado-Rives. 1996. Development and testing of the OPLS all-atom force field on conformational energetics and properties of organic liquids. *J. Am. Chem. Soc.* 118:11225–11236.

63. Ponder, J. W., and D. A. Case. 2003. Force fields for protein simulations. *Adv. Protein Chem.* 66:27–85.

64. Price, D. J., and C. L. Brooks, 3rd. 2002. Modern protein force fields behave comparably in molecular dynamics simulations. *J. Comput. Chem.* 23:1045–1057.

65. Ådén, J., C. F. Weise, …, M. Wolf-Watz. 2013. Structural topology and activation of an initial adenylate kinase-substrate complex. *Biochemistry.* 52:1055–1061.

66. Hammes, G. G., Y.-C. Chang, and T. G. Oas. 2009. Conformational selection or induced fit: a flux description of reaction mechanism. *Proc. Natl. Acad. Sci. USA.* 106:13737–13741.

67. Esteban-Martín, S., R. B. Fenwick, …, X. Salvatella. 2014. Correlated inter-domain motions in adenylate kinase. *PLOS Comput. Biol.* 10:e1003721.

68. Olsson, U., and M. Wolf-Watz. 2010. Overlap between folding and functional energy landscapes for adenylate kinase conformational change. *Nat. Commun.* 1:111.

69. Wolf-Watz, M., V. Thai, …, D. Kern. 2004. Linkage between dynamics and catalysis in a thermophilic-mesophilic enzyme pair. *Nat. Struct. Mol. Biol.* 11:945–949.

70. Sullivan, S. M., and T. Holyoak. 2008. Enzymes with lid-gated active sites must operate by an induced fit mechanism instead of conformational selection. *Proc. Natl. Acad. Sci. USA.* 105:13829–13834.

71. Gunasekaran, K., B. Ma, and R. Nussinov. 2004. Is allostery an intrinsic property of all dynamic proteins? *Proteins.* 57:433–443.

72. Schrank, T. P., D. W. Bolen, and V. J. Hilser. 2009. Rational modulation of conformational fluctuations in adenylate kinase reveals a local unfolding mechanism for allostery and functional adaptation in proteins. *Proc. Natl. Acad. Sci. USA.* 106:16984–16989.

73. Dreusicke, D., P. A. Karplus, and G. E. Schulz. 1988. Refined structure of porcine cytosolic adenylate kinase at 2.1 A resolution. *J. Mol. Biol.* 199:359–371.

74. Mukhopadhyay, A., A. V. Kladova, …, J. Trincão. 2011. Crystal structure of the zinc-, cobalt-, and iron-containing adenylate kinase from *Desulfovibrio gigas*: a novel metal-containing adenylate kinase from Gram-negative bacteria. *J. Biol. Inorg. Chem.* 16:51–61.

75. Schlauderer, G. J., and G. E. Schulz. 1996. The structure of bovine mitochondrial adenylate kinase: comparison with isoenzymes in other compartments. *Protein Sci.* 5:434–441.

76. Müller, C. W., and G. E. Schulz. 1993. Crystal structures of two mutants of adenylate kinase from Escherichia coli that modify the Gly-loop. *Proteins.* 15:42–49.

77. Berry, M. B., E. Bae, …, G. N. Phillips, Jr. 2006. Crystal structure of ADP/AMP complex of *Escherichia coli* adenylate kinase. *Proteins.* 62:555–556.

78. Berry, M. B., B. Meador, …, G. N. Phillips, Jr. 1994. The closed conformation of a highly flexible protein: the structure of *E. coli* adenylate kinase with bound AMP and AMPPNP. *Proteins.* 19:183–198.

79. Bae, E., and G. N. Phillips, Jr. 2004. Structures and analysis of highly homologous psychrophilic, mesophilic, and thermophilic adenylate kinases. *J. Biol. Chem.* 279:28202–28208.

80. Couñago, R., S. Chen, and Y. Shamoo. 2006. In vivo molecular evolution reveals biophysical origins of organismal fitness. *Mol. Cell.* 22:441–449.

81. Abele, U., and G. E. Schulz. 1995. High-resolution structures of adenylate kinase from yeast ligated with inhibitor Ap5A, showing the pathway of phosphoryl transfer. *Protein Sci.* 4:1262–1271.

82. Spuergin, P., U. Abele, and G. E. Schulz. 1995. Stability, activity and structure of adenylate kinase mutants. *Eur. J. Biochem.* 231:405–413.

83. Schlauderer, G. J., K. Proba, and G. E. Schulz. 1996. Structure of a mutant adenylate kinase ligated with an ATP-analogue showing domain closure over ATP. *J. Mol. Biol.* 256:223–227.

84. Wild, K., R. Grafmüller, …, G. E. Schulz. 1997. Structure, catalysis and supramolecular assembly of adenylate kinase from maize. *Eur. J. Biochem.* 250:326–331.

85. Davlieva, M., and Y. Shamoo. 2009. Structure and biochemical characterization of an adenylate kinase originating from the psychrophilic organism Marinibacillus marinus. *Acta Crystallogr. Sect. F Struct. Biol. Cryst. Commun.* 65:751–756.

86. Berry, M. B., and G. N. Phillips, Jr. 1998. Crystal structures of Bacillus stearothermophilus adenylate kinase with bound Ap5A, Mg2+ Ap5A, and Mn2+ Ap5A reveal an intermediate lid position and six coordinate octahedral geometry for bound Mg2+ and Mn2+. *Proteins.* 32: 276–288.

87. Kabsch, W., and C. Sander. 1983. Dictionary of protein secondary structure: pattern recognition of hydrogen-bonded and geometrical features. *Biopolymers.* 22:2577–2637.

88. Hänggi, P., P. Talkner, and M. Borkovec. 1990. Reaction-rate theory: fifty years after Kramers. *Rev. Mod. Phys.* 62:251.

89. Sriraman, S., I. G. Kevrekidis, and G. Hummer. 2005. Coarse master equation from Bayesian analysis of replica molecular dynamics simulations. *J. Phys. Chem. B.* 109:6479–6484.

90. Hummer, G. 2005. Position-dependent diffusion coefficients and free energies from Bayesian analysis of equilibrium and replica molecular dynamics simulations. *New J. Phys.* 7:34.

Supporting Materials

Mapping the Dynamics Landscape of Conformational Transitions in Enzyme: The Adenylate Kinase Case

Dechang Li, Ming S. Liu and Baohua Ji

Contents:

1. **Text S1: Bias-exchange metadynamics method**

The BE-META metadynamics method (1-6) was recently developed in order to accelerate simulations of rare events and to reconstruct the free energy landscape in protein folding (1, 2) and protein ligand-receptor interactions (3). In the metadynamics simulation, the dynamics is performed in the space defined by a few collective variables (CVs) $S\left(\vec{X}\right)$, which are assumed to provide the reaction coordinates of the system and are explicit functions of the system coordinates $\vec{X}$. The dynamics is driven by the free energy function $F\left(S\left(\vec{X}\right)\right)$ and biased by a history-dependent potential $V_G\left(S\left(\vec{X}\right),t\right)$ which is constructed as a sum of Gaussians centered along the trajectory of the CVs:

$$V_G\left(S\left(\vec{X}\right),t\right)=\int_0^t \frac{w}{\tau}\exp\left\{-\frac{\left[S\left(\vec{X}\right)-s(t')\right]^2}{2\sigma^2}\right\}dt' \qquad \text{(S1)}$$

where $s(t')=S\left(\vec{X}(t)\right)$ is the value taken by the CV at time t, w is the height and σ is the width of the Gaussians and τ is the time interval for adding the bias. The bias potential fills the minima along the free energy surface in time, promoting the system to efficiently explore the space defined by the CVs. Given a sufficient long time, $V_G\left(S\left(\vec{X}\right),t\right)\to -F\left(S\left(\vec{X}\right)\right)$.

In the BE-META approach, a large set of CVs is normally chosen to expect to find the accurate free energy landscape of the system. N replicas of MD simulations (walkers) are run in parallel, biasing each walker with a metadynamics bias acting on just one variable. In BE-META the sampling is enhanced by attempting at fixed time intervals of a few picoseconds, and the sampling swaps of the bias potentials between pairs of walkers. The swap is accepted with a probability

$$\min\left\{1,\exp\left[\frac{1}{T}\left(V_G^a\left(S\left(\vec{X}^a\right),t\right)+V_G^b\left(S\left(\vec{X}^b\right),t\right)-V_G^a\left(S\left(\vec{X}^b\right),t\right)-V_G^b\left(S\left(\vec{X}^a\right),t\right)\right)\right]\right\} \qquad \text{(S2)}$$

where $\vec{X}^a$ and $\vec{X}^b$ are the coordinates of walker *a* and *b* and $V_G^{a(b)}\left(S\left(\vec{X}\right),t\right)$ is the metadynamics potential acting on the walker *a* (or *b*). Each walker's trajectory evolves through the high dimensional free energy landscape in the space of the CVs, and it is sequentially biased by different low dimensional potentials acting on one CV at each time. The swaps greatly increase the replicas to diffuse in the CV space. The results of the simulation are N low dimensional projections of the free energy. The multi dimensional free energy landscape can be obtained through a weighted-histogram procedure by clustering the replica trajectories together. (1) More details of the BE-META simulation method can be found in the work by Laio and co-workers (1-6).

In this study, three set of CVs has been selected as putative reaction coordinates to explore the conformational transition pathway of AdK: a) the angle LID- CORE θ_1, b) the angle NMP-CORE θ_2 and c) the distance between group LID and NMP d_{LN}, as shown in Figure 1 of the main text. The parameters adopted in the BE-META simulations are as following: Gaussian height 0.05 kcal/mol, Gaussian widths equal to

0.01 radian for θ_1 and θ_2, and 0.1 Å for d_{LN}, deposition of a Gaussian every 1 ps, swaps of bias attempted every 2 ps. To reduce the computational cost and maintain the reasonable conformation of AdK, walls have been set on three CVs to restrict them in a reasonable zone: $58^\circ \le \theta_1 \le 100^\circ$, $20^\circ \le \theta_2 \le 70^\circ$ and $15\text{Å} \le d_{LN} \le 45\text{Å}$.

BE-META simulations were performed biasing each of three CVs on a different replica (plus one replica without any bias) for a total of 200 ns per replica, thus a total 800ns time scale per BE-META simulation in this study, as described in Table S1. Simulations first equilibrate in NPT ensemble at 300K and 1 bar. After 1ns of equilibration, the barostat was removed and the BE-META simulation was started. The atomic coordinates were saved every 5ps and the energy saved every 0.05 ps. The BE-META simulations were performed with GROMACS (7, 8) plus PLUMED package (9), and the results were analyzed using METAGUI (10) developed by Laio and co-works (1-6) on VMD program (11).

2. Text S2: Conformational Transitions in AdK as determined by explicit long-time MD (LT-MD) simulations

LT-MD simulations starting from the open state without ligands

Figure S1 showed the Simulation #O_1 results of conformational evolution of AdK starting from the open state without ligands. The angle LID-CORE θ_1 rapidly decreases from $\sim 95^\circ$ to $\sim 70^\circ$ in ~10ns, indicating that the LID domain closes during this time. However, the angle NMP-CORE θ_2 is stabilized at $\sim 60^\circ$ through all the 1000ns simulation time. After about 100ns, angle θ_1 increases to $\sim 100^\circ$ again and the LID domain open, as shown in Figure S1 (a) and (b) at t = 134ns. Along with the closing of LID domain, the distance between LID and NMP d_{LN} decreases to $\sim 25\text{Å}$ firstly and then decreases further to $\sim 20\text{Å}$. The above results indicate that the LID domain is much flexible and can close rapidly at time scale of a few nanoseconds. Besides, the LID domain not only closes to the CORE domain, but also moves toward to the NMP domain, see Figure S1 (b). The RMSD results show that the starting open conformation deviates from the initial state and close to the closed conformation. However, at the end of 1000ns simulation, the conformation of AdK did not reach the crystal closed state because of the opening of NMP domain.

To confirm the conformational transitions of AdK starting from the open state, we did two more simulations with the same initial coordinates but different initial velocity of the atoms. Simulation #O_2 starting from open state without ligands showed that the LID domain closed at about ~13ns. At the same time, the distance between LID and NMP d_{LN} decreases to $\sim 16\text{Å}$, showing that the LID and NMP domain contact well because of the closure of the LID domain. After the closure of the LID domain, θ_2 decreases gradually to $\sim 35^\circ$ in 50ns. Hereafter, we refer the above conformation when $\theta_2 \approx 35^\circ \sim 45^\circ$ as a semi-open state of the NMP domain. After the contact between the LID and NMP domain, the conformation of AdK is trapped at an intermediate state that

$\theta_1 \approx 60^\circ$, $\theta_2 \approx 35^\circ \sim 45^\circ$ and $d_{LN} \approx 16\text{Å} \sim 30\text{Å}$, as shown in Figure S2. Simulation #O_3 starting from open state without ligands shows similar behaviors that the LID domain closes gradually in ~60ns time scale. Before the closure of the LID domain, the NMP domain fluctuates from $\sim 60^\circ$ (open) to $\sim 45^\circ$ (semi-open), as shown in Figure S3 at t ~30ns. After the LID domain closes, the NMP domain still remains in the open state. Similarly, the distance between LID and NMP d_{LN} decreases to $16\text{Å} \sim 30\text{Å}$ and maintains this value, see Figure S3.

The above simulations starting from the open state without ligands show that the LID domain is much more flexible than NMP, able to be closed at the time scale ~10ns. There is one of the three simulations observed the NMP domain closed after the motions of LID, at the time scale ~100ns, but not as closed as the crystal conformation of 1AKE (as shown in Figure S2 at t=160ns). Interestingly, all of the three simulations observed the intermediate conformation that the LID domain not only closes to CORE domain, but also contacts well with the NMP domain (even with the NMP domain opening), as shown in the snapshots in Figure S1 (b) (also see Figure S2 (b) and Figure S3 (b)). None of the three simulations observed the crystal closed conformation, because of the open state of NMP domain.

LT-MD simulations starting from the closed state without ligands

Figure S4 shows the Simulation #C_1 results of the conformational evolution of AdK starting from the closed state without ligands. As shown in Figure S4 (a), the angle NMP-CORE θ_2 fluctuates from $\sim 30^\circ$ to $\sim 45^\circ$ (semi-open state) in the time scale ~10ns before ~70ns. During the fluctuation of NMP domain, the LID domain takes an open conformation, as shown in Figure S4 at t = 56.3ns. The conformation at t = 56.3ns is similar to the crystal structure of 4AKE, as RMSD with reference to the open conformation decreases to $\sim 3\text{Å}$. At the time 70ns ~ 75ns, the angle NMP-CORE θ_2 increases from $\sim 30^\circ$ to $\sim 45^\circ$ in the first step (semi-open state), and then further increases from $\sim 45^\circ$ to $\sim 60^\circ$ for fully open in the second step. After the fully opening of the NMP domain, the LID domain stays at the closed state and maintains the contact with the NMP domain, as $d_{LN} \approx 16\text{Å}$ in Figure S4 (a). At time 400ns ~ 440ns, the LID domain opens again (Figure S4). More importantly, the simulation shows that the NMP domain can re-close after its opening at a long time scale simulation. In Figure S4 (a) at t = 800ns, the result clearly shows that θ_2 decreases from $\sim 60^\circ$ (open) to $\sim 40^\circ$ (semi-open). Before the closing of the NMP domain, we see that the contact between the LID and NMP domain becomes unstable as d_{LN} fluctuates from $\sim 16\text{Å}$ to $\sim 30\text{Å}$. The fluctuation indicates that at this time the LID domain moves toward to the CORE domain and the contact is broken, thus the NMP domain can move to the semi-open state.

Simulation #C_1 (starting from the closed conformation without ligands) shows that the closed to the open transition starts by the opening of NMP domain first. However, Simulation #C_2 with the same initial coordinate but different initial velocity of the atoms shows a clearly alternative pathway. It shows that the LID domain opens first at ~5ns. After the opening of LID domain, the NMP domain remains closed till

~30ns and then opens up rapidly, as shown in Figure S5. Simulation #C_2 shows the transition pathway is LID opens first and then NMP opens. Simulation #C_3 also shows the NMP domain can open when the LID domain is closed, as shown in Figure S6. Interestingly, Simulation #C_3 shows that the NMP domain finally is closed to $\theta_2 \approx 35^\circ$ when the LID domain at $\theta_1 \approx 60^\circ$ in the time scale ~250ns. This conformation is more compact than that of the crystal structure 1AKE (with ligands).

The above simulations show that the closed conformation of AdK can transforms to open one at ~10ns time scale without the ligands. The simulations represent at least two complete distinguishing conformational transition pathways. One is the NMP domain opens first and then the LID domain opens. The other pathway is in the opposite order.

LT-MD simulations with ligands

To check the conformational dynamics mechanism of AdK induced by ligands, we considered the conformational transitions of AdK starting from the open and closed states with various ligands, such as with both ATP and AMP, only ATP and only AMP. Figure S7 shows the simulation results of the conformational evolution of AdK starting from the open state with both ATP and AMP. As shown in Figure S7, with the ligands of ATP and AMP, the LID domain can close from the open state rapidly with the motion similar to the simulations without ligands (see Figure S1). The NMP domain can close to its intermediate state (i.e. $\theta_2 \approx 45^\circ$) much faster than that without ligands, i.e. with the time scale ~50~100 ns, as shown in Figure S7. However, at the end of 1000ns simulation, AdK did not transform to the closed conformation as in the crystal structure of 1AKE, because of the semi-open state of NMP is stable. The simulation of AdK with only ATP shows similar conformational transitions that the LID domain closes rapidly, while the NMP domain only fluctuates to the semi-open state but not fully closes, as shown in Figure S8. Figure S9 shows the simulation result with only AMP, which shows more various conformational transitions. Firstly, when binding with AMP, the LID domain closes to $\theta_1 \approx 70^\circ$ at ~5ns. In the second step, the LID domain closes further from $\theta_1 \approx 70^\circ$ to $\theta_1 \approx 60^\circ$ at ~30ns. After the closure of the LID domain, the NMP domain closes gradually from $\theta_2 \approx 70^\circ$ to $\theta_2 \approx 50^\circ$. Finally, the LID and NMP domain form contact with $d_{LN} \approx 18$Å at ~90ns and the conformation is stabilized as a closed state through to the end of the simulation.

When starting from the closed state with both ATP and AMP, the structure is stabilized at the crystal closed conformation as expected, i.e. the angle θ_1 and θ_2 are stabilized around $\sim 65^\circ$ and $\sim 30^\circ$, respectively, as shown in Figure S10. However, after ~125ns simulation, the NMP domain presents a significant motion as the NMP-CORE angle θ_2 increases from $\sim 30^\circ$ to $\sim 45^\circ$ in a few nanoseconds.

3. Text S3: The calculation of the transition rate constants

We estimated the transition rate constants based on Kramers' transition state theory (12). We assumed that the diffusion coefficients are the same along the two reaction coordinates (i.e. θ_1 and θ_2 in Figure 5 and 6 of the manuscript), which can be estimated directly through the LT-MD simulations (13, 14).

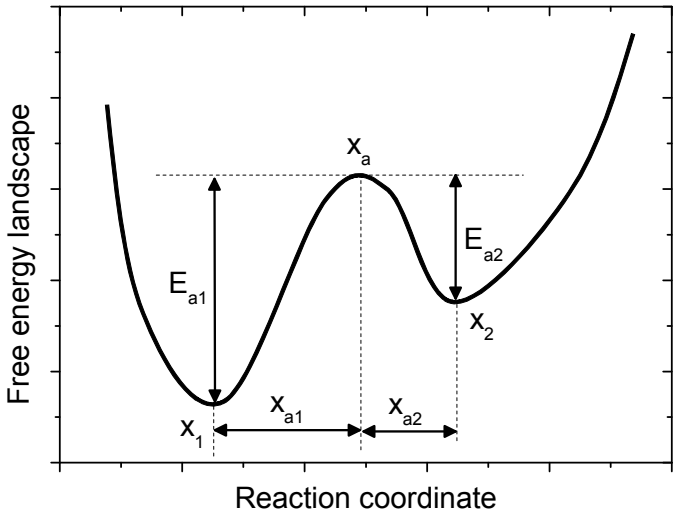

Figure S0. Illustration of the transition between two states.

As shown in Figure S0, we define the rate constants of transition between the two states:

$$k_{12} = k_{1\to 2} \tag{S3}$$

$$k_{21} = k_{2\to 1} \tag{S4}$$

The transition from State 1 to State 2 can be thought of as a two step process: first reach to the activation point x_a and then enter State 2 from x_a. Denoting the probability of actual transition into State 2 from x_a is ε_{12}, we can write

$$k_{12} = \varepsilon_{12}\frac{1}{t_{K1}} \tag{S5}$$

where t_{K1} is the Kramer time of reaching the activation point x_a from x_1. Similarly, for transition from State 2 to State 1, we have

$$k_{21} = \varepsilon_{21}\frac{1}{t_{K2}} \tag{S6}$$

obviously,

$$\varepsilon_{12} + \varepsilon_{21} = 1 \tag{S7}$$

For detailed balance, we have

$$k_{12}C_1 = k_{21}C_2 \tag{S8}$$

where C_1 and C_2 is the probability in State 1 and State 2, respectively. According to the Maxwell-Boltzmann distribution

$$\frac{C_2}{C_1}=\frac{\exp\left(-G_2/k_BT\right)}{\exp\left(-G_1/k_BT\right)}=\exp\left(-\Delta G_{21}/k_BT\right) \tag{S9}$$

here $\Delta G_{21}=G_2-G_1$ is the difference in free energy between State 1 and State 2. Therefore,

$$\frac{k_{12}}{k_{21}}=\frac{C_2}{C_1}=\exp\left(-\Delta G_{21}/k_BT\right) \tag{S10}$$

On the other hand,

$$t_K=\frac{1}{D}\int_{well}\exp\left(-\frac{\Delta G(x)}{k_BT}\right)dx\int_{barrier}\exp\left(\frac{\Delta G(x)}{k_BT}\right)dx \tag{S11}$$

Assuming that the energy well in State 1 and State 2 are harmonic types, while $E_{a1}>>k_BT$ and $E_{a2}>>k_BT$, we have

$$t_{K1}=\frac{x_{a1}^2}{2D}\cdot\pi^{1/2}\cdot\left(\frac{E_{a1}}{k_BT}\right)^{-3/2}\cdot\exp\left(\frac{E_{a1}}{k_BT}\right) \tag{S12}$$

$$t_{K2}=\frac{x_{a2}^2}{2D}\cdot\pi^{1/2}\cdot\left(\frac{E_{a2}}{k_BT}\right)^{-3/2}\cdot\exp\left(\frac{E_{a2}}{k_BT}\right) \tag{S13}$$

$$\frac{k_{12}}{k_{21}}=\frac{\varepsilon_{12}}{\varepsilon_{21}}\cdot\frac{t_{K2}}{t_{K1}}=\frac{\varepsilon_{12}}{\varepsilon_{21}}\cdot\frac{\left(E_{a1}\right)^{3/2}x_{a2}^2}{\left(E_{a2}\right)^{3/2}x_{a1}^2}\cdot\exp\left(-\frac{\Delta G_{21}}{k_BT}\right) \tag{S14}$$

here x_{a1} and x_{a2} are the distance between activation point x_a and the energy well 1 and 2, respectively. E_{a1} and E_{a2} are the energy barriers between activation point x_a and the energy well 1 and 2. The parameter D is the diffusion coefficient. It should be noted that the analytical results of t_{K1} and t_{K2} in eq. S12 and S13 are only validated when $E_{a1}>>k_BT$ and $E_{a2}>>k_BT$. If $E_{a1}\sim k_BT$ or $E_{a2}\sim k_BT$, eq. S11 can be integrated numerically to obtain t_{K1} and t_{K2}.

Finally, we can find that

$$\varepsilon_{12}=\frac{\left(E_{a2}\right)^{3/2}x_{a1}^2}{\left(E_{a1}\right)^{3/2}x_{a2}^2+\left(E_{a2}\right)^{3/2}x_{a1}^2} \tag{S15}$$

$$\varepsilon_{21}=\frac{\left(E_{a1}\right)^{3/2}x_{a2}^2}{\left(E_{a1}\right)^{3/2}x_{a2}^2+\left(E_{a2}\right)^{3/2}x_{a1}^2} \tag{S16}$$

thus

$$k_{12}=\varepsilon_{12}\frac{1}{t_{K1}}=\frac{2D}{\sqrt{\pi}}\frac{\left(E_{a2}\right)^{3/2}}{\left(E_{a1}\right)^{3/2}x_{a2}^2+\left(E_{a2}\right)^{3/2}x_{a1}^2}\left(\frac{E_{a1}}{k_BT}\right)^{\frac{3}{2}}\exp\left(-\frac{E_{a1}}{k_BT}\right) \tag{S17}$$

$$k_{21}=\varepsilon_{21}\frac{1}{t_{K2}}=\frac{2D}{\sqrt{\pi}}\frac{\left(E_{a1}\right)^{3/2}}{\left(E_{a1}\right)^{3/2}x_{a2}^2+\left(E_{a2}\right)^{3/2}x_{a1}^2}\left(\frac{E_{a2}}{k_BT}\right)^{\frac{3}{2}}\exp\left(-\frac{E_{a2}}{k_BT}\right) \tag{S18}$$

According to equation (S17) and (S18), we can calculate the transition rate constants. It should be noted that in real system the diffusion behavior could be anisotropy, and the diffusion coefficient should depend on the starting position (14). But position-dependent diffusion coefficient will bring in too much complexity and errors for calculating the transition rates (1). Our treatment is to calculate the rates of transition between the two states, neglecting the position-dependence of diffusion coefficient.

4. Text S4: Calculation of proportion of different pathways

According to Hammes (1), the fractional flux through a given pathway is a precise measure of how much a transition proceeds through that path. For a serial transition pathway, the total flux can be calculated as

$$F_{total} = \left(\sum 1/F_{ij} \right)^{-1} \tag{S19}$$

Where F_{total} is the total flux through a specified serial pathway and F_{ij} is the flux from state *i* to state *j*:

$$F_{ij} = k_{ij} C_i \tag{S20}$$

Where k_{ij} is the transition rate constant from state i to state j, and C_i is the concentration in state i, respectively. The proportion of the concentration in state i and j is related to their relative free energy

$$\frac{C_i}{C_j} = \frac{\exp\left(-\Delta G_i / k_B T\right)}{\exp\left(-\Delta G_j / k_B T\right)} = \exp\left[-\frac{\Delta G_i - \Delta G_j}{k_B T} \right] \tag{S21}$$

While in an equilibrium ensemble, the flux should balance between state i and j (also see eq. S8 in the method of the transition rate calculation in Supporting Materials),

$$F_{ij} = F_{ji} \tag{S22}$$

The total flux of AdK's conformational transition starting from open to closed through a specified serial pathway, e.g., $\alpha \to \beta \to \gamma \to \delta \to \xi$ in Figure 5C, can be calculated as

$$F_{\alpha\to\beta\to\gamma\to\delta\to\xi} = \left(\frac{1}{k_{\alpha\beta} C_\alpha} + \frac{1}{k_{\beta\gamma} C_\beta} + \frac{1}{k_{\gamma\delta} C_\gamma} + \frac{1}{k_{\delta\xi} C_\delta} \right)^{-1} \tag{S23}$$

Similarly, the total flux of the reverse direction of the same pathway, i.e., $\xi \to \delta \to \gamma \to \beta \to \alpha$ in Figure 5C, can be calculated as

$$F_{\xi\to\delta\to\gamma\to\beta\to\alpha}=\left(\frac{1}{k_{\xi\delta}C_{\xi}}+\frac{1}{k_{\delta\gamma}C_{\delta}}+\frac{1}{k_{\gamma\beta}C_{\gamma}}+\frac{1}{k_{\beta\alpha}C_{\beta}}\right)^{-1} \tag{S24}$$

For equilibrium ensemble, the flux between neighboring states satisfy

$$k_{\alpha\beta}C_{\alpha}=k_{\beta\alpha}C_{\beta} \tag{S25.a}$$

$$k_{\beta\gamma}C_{\beta}=k_{\gamma\beta}C_{\gamma} \tag{S25.b}$$

$$k_{\gamma\delta}C_{\gamma}=k_{\delta\gamma}C_{\delta} \tag{S25.c}$$

$$k_{\delta\xi}C_{\delta}=k_{\xi\delta}C_{\xi} \tag{S25.d}$$

As a result, the proportion of the forward and backward transitions in the same pathway $\alpha\to\beta\to\gamma\to\delta\to\xi$ is given:

$$\frac{F_{\alpha\to\beta\to\gamma\to\delta\to\xi}}{F_{\xi\to\delta\to\gamma\to\beta\to\alpha}}=\left(\frac{1}{k_{\alpha\beta}C_{\alpha}}+\frac{1}{k_{\beta\gamma}C_{\beta}}+\frac{1}{k_{\gamma\delta}C_{\gamma}}+\frac{1}{k_{\delta\xi}C_{\delta}}\right)^{-1}\Bigg/\left(\frac{1}{k_{\xi\delta}C_{\xi}}+\frac{1}{k_{\delta\gamma}C_{\delta}}+\frac{1}{k_{\gamma\beta}C_{\gamma}}+\frac{1}{k_{\beta\alpha}C_{\beta}}\right)^{-1}=1 \tag{S26}$$

The above result concludes that the proportion of the transitions in the forward and backward direction in the same pathway is identical the same.

In another word, we can calculate the proportion of the transitions between individual pathways. For AdK, one of the conformation transition pathways starting from open to closed state is that LID closes first and then NMP closes afterward, i.e., $\alpha\to\beta\to\gamma\to\delta\to\xi$. The flux through this pathway is

$$F_{\alpha\to\beta\to\gamma\to\delta\to\xi}=\left(\frac{1}{k_{\alpha\beta}C_{\alpha}}+\frac{1}{k_{\beta\gamma}C_{\beta}}+\frac{1}{k_{\gamma\delta}C_{\gamma}}+\frac{1}{k_{\delta\xi}C_{\delta}}\right)^{-1} \tag{S27}$$

The other pathway is that NMP closes first and then LID closes afterward, i.e., $\alpha\to\beta\to\varepsilon\to\xi$. The flux through this pathway can be calculated as

$$F_{\alpha\to\beta\to\varepsilon\to\xi}=\left(\frac{1}{k_{\alpha\beta}C_{\alpha}}+\frac{1}{k_{\beta\varepsilon}C_{\beta}}+\frac{1}{k_{\varepsilon\xi}C_{\varepsilon}}\right)^{-1} \tag{S28}$$

Thus the proportion of the transitions between these two pathways is

$$\frac{F_{\alpha\to\beta\to\gamma\to\delta\to\xi}}{F_{\alpha\to\beta\to\varepsilon\to\xi}}=\left(\frac{1}{k_{\alpha\beta}C_{\alpha}}+\frac{1}{k_{\beta\gamma}C_{\beta}}+\frac{1}{k_{\gamma\delta}C_{\gamma}}+\frac{1}{k_{\delta\xi}C_{\delta}}\right)^{-1}\Bigg/\left(\frac{1}{k_{\alpha\beta}C_{\alpha}}+\frac{1}{k_{\beta\varepsilon}C_{\beta}}+\frac{1}{k_{\varepsilon\xi}C_{\varepsilon}}\right)^{-1}\approx\frac{5.7}{1} \quad \text{(S29)}$$

The above result shows that the transition of AdK mainly follows the pathways that LID closes first and then NMP closes afterward, which is consistent with Esteban-Martin et al.'s experimental work for the case of unbound state (2).

5. Supporting tables

Table S1. Conformational states of AdK without ligands as in crystal structures.

Protein	Organism	Ligand	PDB ID	Angles		Reference
				θ_1 (°)	θ_2 (°)	
AdK	E. coli	-	4AKE	95.0	60.9	Müller et al. (15)
AdK	A. aeolicus	-	2RH5	93.0	63.0	Henzler-Wildman et al. (16)
AdK	Vibrio cholerae	-	4NP6	93.5	60.5	Kim et al., unpublished results
AdK	Sus scrofa	-	3ADK	97.0	44.9	Dreusicke et al. (17)
AdK	Thermus thermophilus	-	3CM0	97.1	61.9	Nakagawa et al., unpublished results
AdK	D. gigas	-	3L0P	84.8	51.5	Mukhopadhyay et al. (18)
AdK	D. gigas	-	3L0S	78.8	52.5	Mukhopadhyay et al. (18)
AdK	D. gigas	-	2XB4	78.7	51.8	Mukhopadhyay et al. (18)
AdK4	H. sapiens	-	2AR7	98.3	62.2	Filippakopoulos et al., unpublished results
AdKiso2	B. taurus mitochondria	-	1AK2	66.8	59.2	Schlauderer and Schulz (19)
AdKiso2	B. taurus mitochondria	-	2AK2	66.3	58.9	Schlauderer and Schulz (19)

Table S2. Conformational states of AdK with ligands as in crystal structures.

Protein	Organism	Ligand	PDB ID	Angles		Reference
				θ_1	θ_2	
AdK	E. coli	Ap_5A	1AKE	69.1	28.6	Müller and Schulz (20)
AdK	E. coli	Ap_5A	1E4V	62.6	26.5	Müller and Schulz (21)
AdK	E. coli	Ap_5A	1E4Y	58.9	26.0	Müller and Schulz (21)
AdK	E. coli	Ap_5A	3HPQ	63.3	28.3	Schrank et al. (22)
AdK	E. coli	Ap_5A	3HPR	63.4	28.1	Schrank et al. (22)
AdK	E. coli	ADP, AMP	2ECK	62.3	27.2	Berry et al. (23)
AdK	E. coli	ANP, AMP	1ANK	62.8	27.1	Berry et al. (24)
AdK	B. globisporus	Ap_5A	1S3G	63.7	28.3	Bae and Phillips (25)
AdK	B. subtilis	Ap_5A	1P3J	64.3	28.3	Bae and Phillips (25)
AdK	B. subtilis	Ap_5A	2EU8	65.5	27.8	Counago et al. (26)
AdK	B. subtilis	Ap_5A	2P3S	65.5	28.9	Counago et al., unpublished results
AdK	B. subtilis	Ap_5A	2OO7	65.5	28.1	Counago et al., unpublished results
AdK	B. subtilis	Ap_5A	2ORI	65.6	27.5	Counago et al., unpublished results
AdK	B. subtilis	Ap_5A	2OSB	65.5	27.78	Counago et al., unpublished results
AdK	B. subtilis	Ap_5A	2QAJ	63.9	29.0	Counago et al., unpublished result

Table S2 continued.

Protein	Organism	Ligand	PDB ID	Angles		Reference
				θ_1	θ_2	
AdK	B. subtilis	Ap_5A	3DKV	63.3	28.4	Bannen et al., unpublished result
AdK	B. subtilis	Ap_5A	3DL0	64.5	28.3	Bannen et al., unpublished result
AdK	A. aeolicus	Ap_5A	2RGX	68.7	28.1	Henzler-Wildman et al. (16)
AdK	A. aeolicus	AMP, ADP, ALF	3SR0	67.2	27.6	Cho and Kern, unpublished result
AdK	S. cerevisiae	Ap_5A	1AKY	64.3	25.3	Abele and Schulz (27)
AdK	S. cerevisiae	Ap_5A	2AKY	63.8	26.9	Abele and Schulz (27)
AdK	S. cerevisiae	Ap_5A	3AKY	64.4	26.7	Spuergin et al. (28)
AdK	S. cerevisiae	ATF	1DVR	61.7	56.9	Schlauderer et al. (29)
AdK	Z. mays	Ap_5A	1ZAK	63.7	28.7	Wild et al. (30)
AdK	J. marinus	Ap_5A	3FB4	63.3	27.6	Davlieva and Shamoo (31)
AdK	B. stearothermophilus	Ap_5A	1ZIN	72.3	28.3	Berry and Phillips (32)
AdK	B. stearothermophilus	Ap_5A	1ZIO	73.1	28.2	Berry and Phillips (32)
AdK	B. stearothermophilus	Ap_5A	1ZIP	72.5	28.2	Berry and Phillips (32)
AdK4	H. sapiens	Gp_5G	2BBW	81.9	44.4	Filippakopoulos et al., unpublished results
AdKiso2	H. sapiens mitochondria	Ap_4A	2C9Y	70.5	59.8	Bunkoczi et al., unpublished results

Table S3. Conformational transitions and pathways in AdK as determined by LT-MD simulations.

Starting States	Ligands	Simulation Method (trajectory #)	Observed conformational transitions and pathways	Total simulation time (ns)
'Open' structure (e.g. PDB: 4AKE)	none	LT-MD (simulation #O_1)	LID open ↔ LID closed	1000
	none	LT-MD (simulation #O_2)	1st step: LID open → LID closed 2nd step: NMP open → NMP semi-open	300
	none	LT-MD (simulation #O_3)	1st step: NMP open ↔ NMP semi-open 2nd step: LID open → LID closed	200
	ATP•Mg^{2+}•AMP	LT-MD (simulation #O-ATP-AMP)	1st step: LID open → LID closed 2nd step: NMP open ↔ NMP semi-open	1000
	ATP•Mg^{2+}	LT-MD (simulation #O-ATP)	1st step: LID open → LID closed 2nd step: NMP open ↔ NMP semi-open	1000
	Mg^{2+}•AMP	LT-MD (simulation #O-AMP)	1st step: LID open → LID closed 2nd step: NMP open ↔ NMP semi-open	1000
'Closed' structure (e.g. PDB 1AKE)	none	LT-MD (simulation #C_1)	a) 1st step: NMP closed ↔ NMP semi-open ↔ NMP open 2nd step: LID closed ↔ LID open b) NMP open → NMP semi-open	1000
	none	LT-MD (simulation #C_2)	1st step: LID closed → LID open 2nd step: NMP closed → NMP open	300
	none	LT-MD (simulation #C_3)	NMP closed → NMP semi-open → NMP open → NMP semi-open	300

	ATP•Mg^{2+}•AMP	LT-MD (simulation #C-ATP-AMP)	NMP closed → NMP semi-open	1000

Table S4. The setup of BE-META simulations.

	Starting States of each replicas	Ligands	Total simulation time of each replicas (ns)
Unbound AdK	'Open' structure PDB: 4AKE	None	200
	'Open' structure PDB: 4AKE	None	200
	'Closed' structure PDB: 1AKE	None	200
	'Closed' structure PDB: 1AKE	None	200
Bound AdK	'Closed' structure PDB: 1AKE	ATP•Mg^{2+}•AMP	200
	'Closed' structure PDB: 1AKE	ATP•Mg^{2+}•AMP	200
	'Closed' structure PDB: 1AKE	ATP•Mg^{2+}•AMP	200
	'Closed' structure PDB: 1AKE	ATP•Mg^{2+}•AMP	200

6. Supporting figures

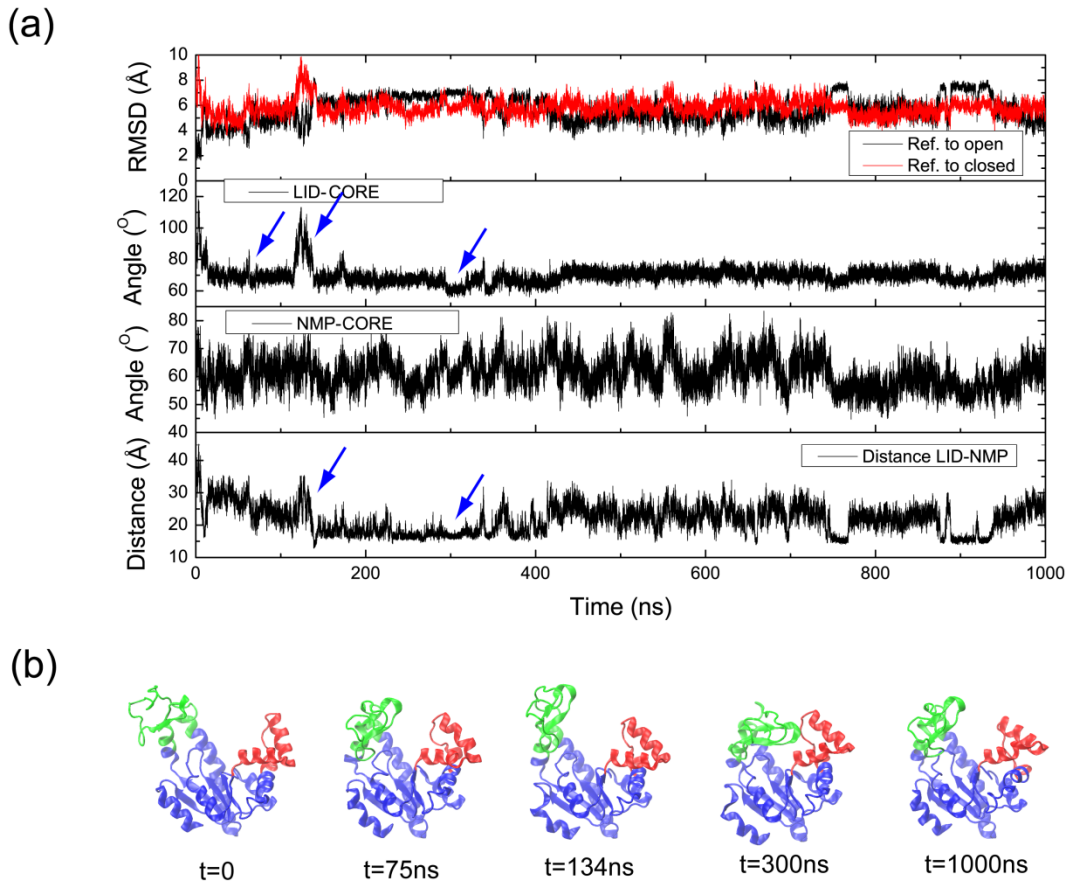

Figure S1. Conformational evolution of AdK starting from the open state without ligands, Simulation #O_1. (a) The evolution of the four variables during the simulation: RMSD reference to open (black curve) and closed (red curve) conformation, Angle of LID-CORE θ_1, Angle of NMP-CORE θ_2 and the distance between LID and NMP d_{LN}. The arrows highlight the events of conformational transitions. (b) Snapshots of the conformational states during the simulation.

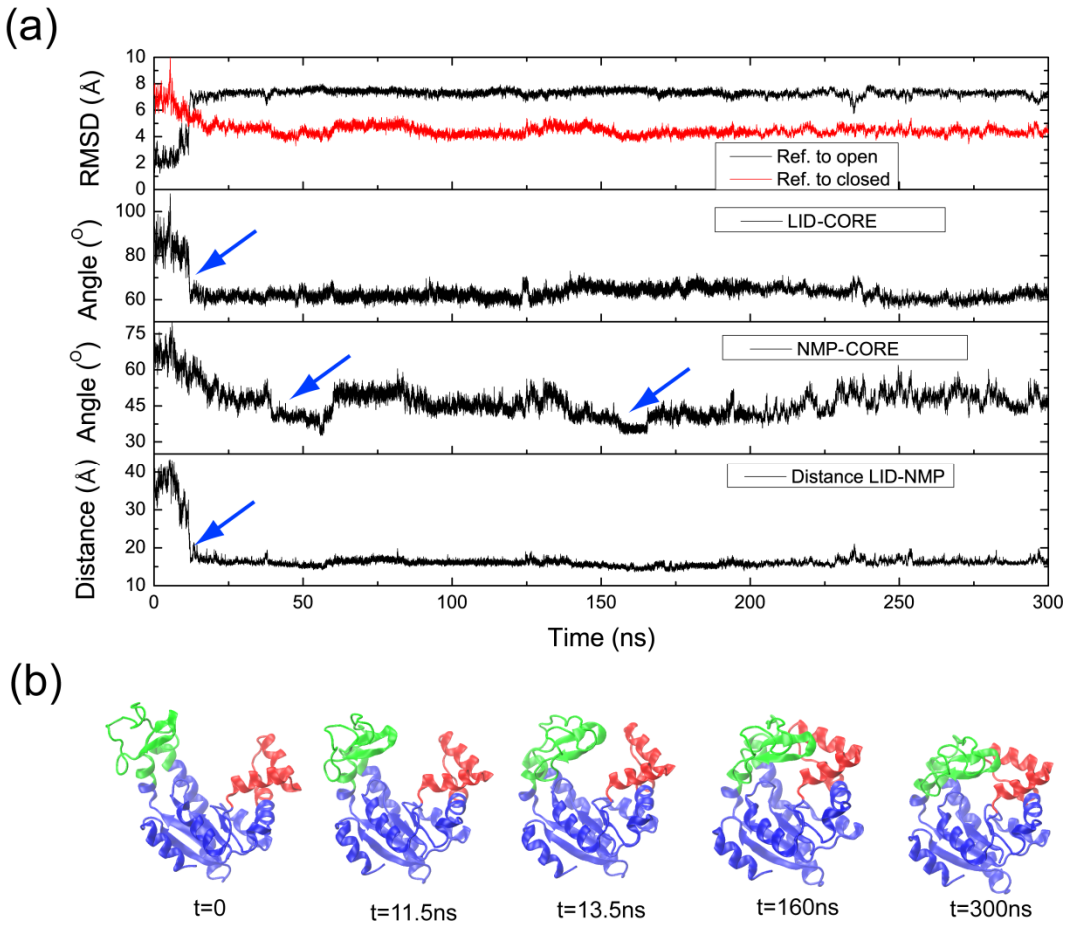

Figure S2. Conformational evolution of AdK starting from the open state without ligands, Simulation #O_2. (a) The evolution of the four variables during the simulation: RMSD reference to open (black curve) and closed (red curve) conformation, Angle of LID-CORE θ_1, Angle of NMP-CORE θ_2 and the distance between LID and NMP d_{LN}. The arrows highlight the events of conformational transitions. (b) Snapshots of the conformational changes during the simulation.

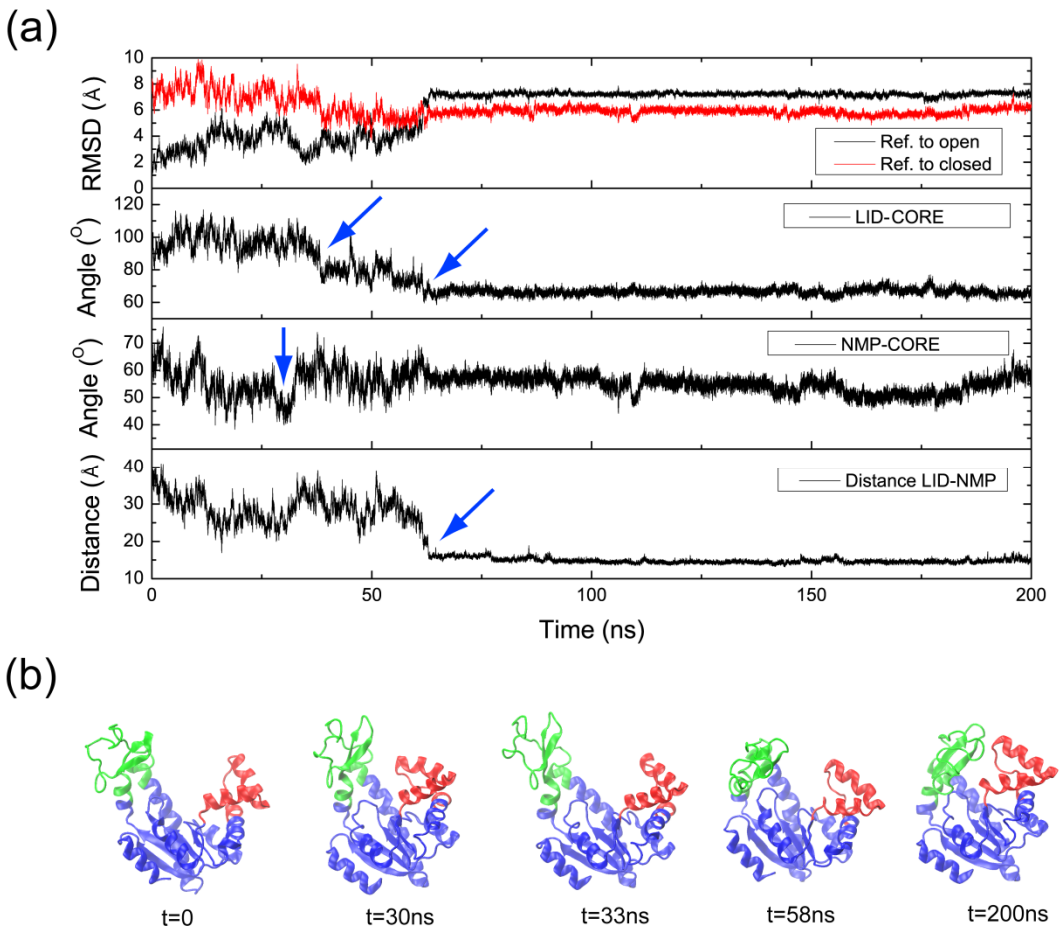

Figure S3. Conformational evolution of AdK starting from the open state without ligands, Simulation #O_3. (a) The evolution of the four variables during the simulation: RMSD reference to open (black curve) and closed (red curve) conformation, Angle of LID-CORE θ_1, Angle of NMP-CORE θ_2 and the distance between LID and NMP d_{LN}. The arrows highlight the events of conformational transitions. (b) Snapshots of the conformational changes during the simulation.

(a)

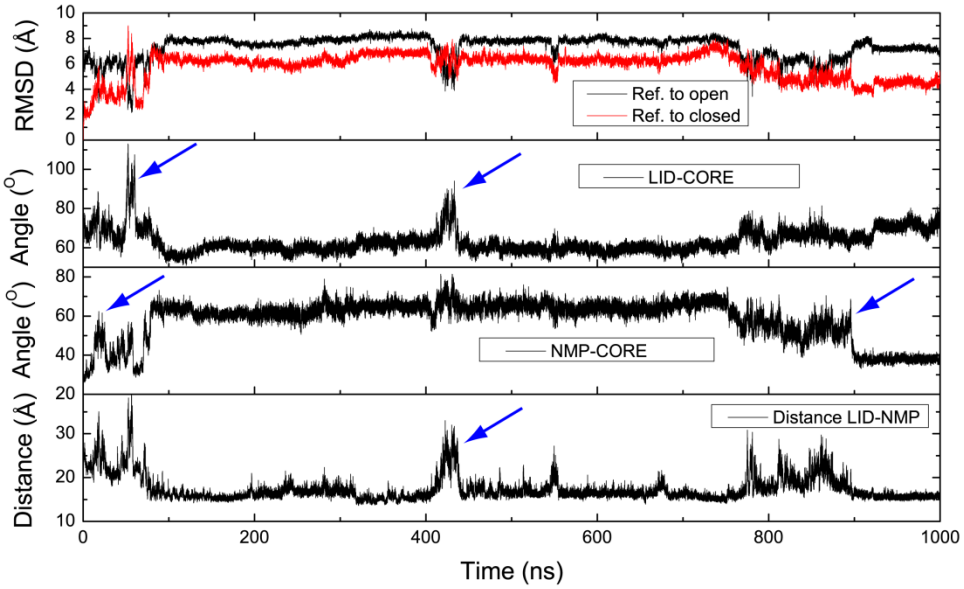

(b)

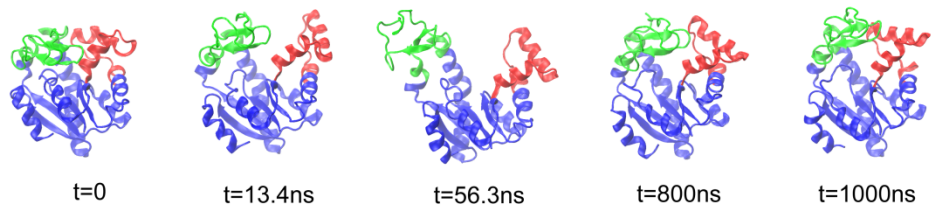

Figure S4. Conformational evolution of AdK starting from the closed state without ligands, Simulation #C_1. (a) The evolution of the four variables during the simulation: RMSD reference to open (black curve) and closed (red curve) conformation, Angle of LID -CORE θ_1, Angle of NMP-CORE θ_2 and the distance between LID and NMP d_{LN}. The arrows highlight the events of conformational transitions. (b) Snapshots of the conformational changes during the simulation.

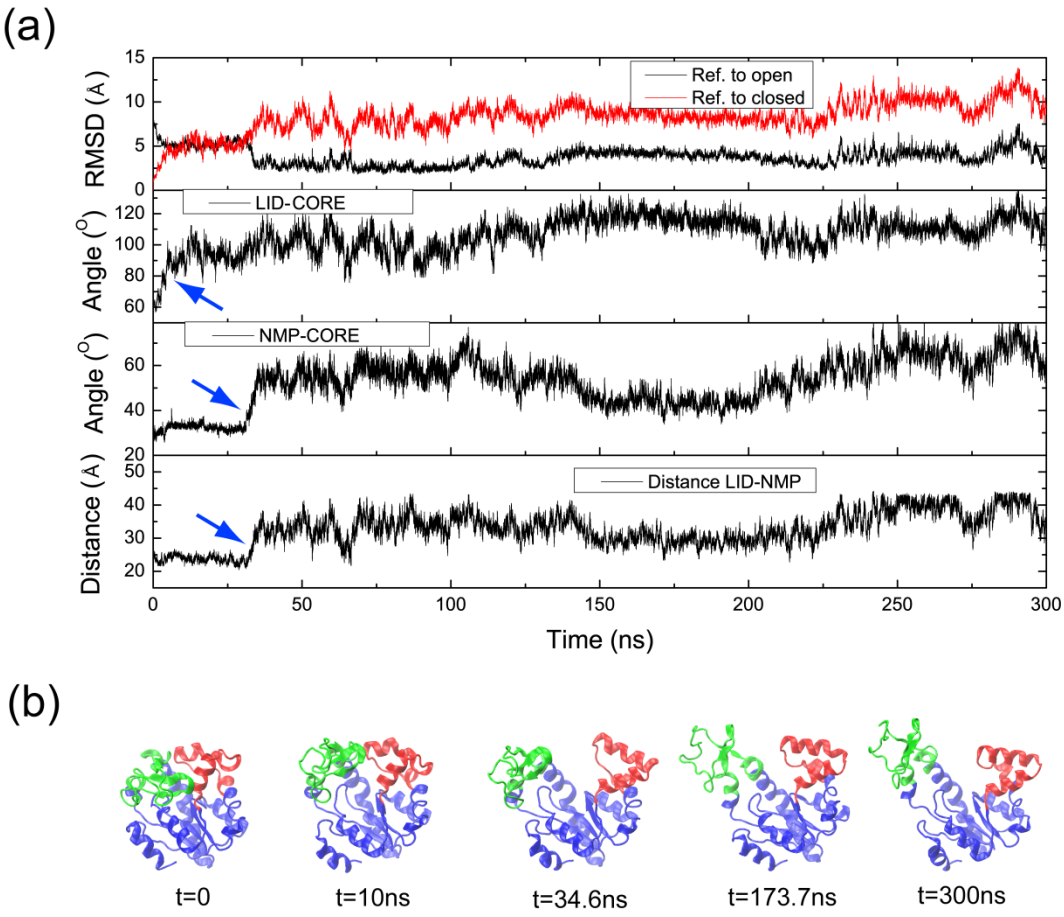

Figure S5. Conformational evolution of AdK starting from the closed state without ligands, Simulation #C_2. (a) The evolution of the four variables during the simulation: RMSD reference to open (black curve) and closed (red curve) conformation, Angle of LID-CORE θ_1, Angle of NMP-CORE θ_2 and the distance between LID and NMP d_{LN}. The arrows highlight the events of conformational transitions. (b) Snapshots of the conformational changes during the simulation.

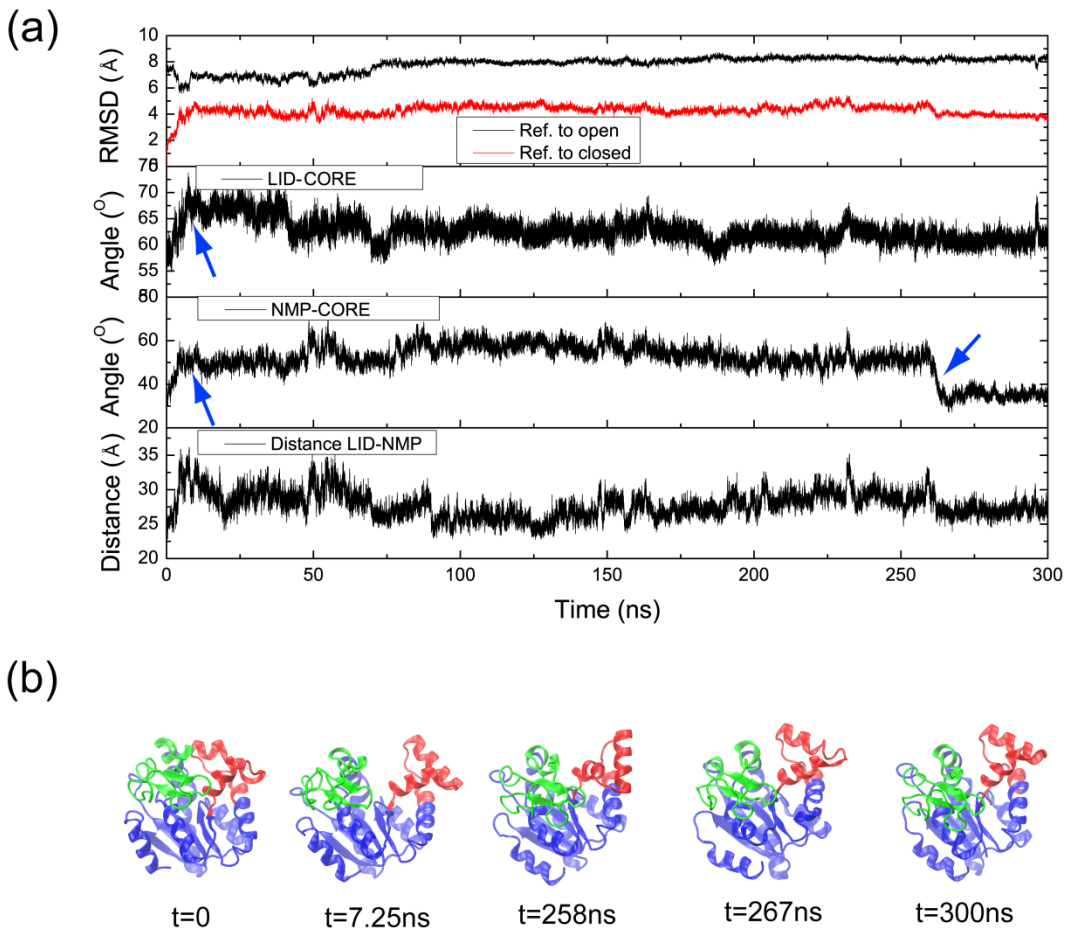

Figure S6. Conformational evolution of AdK starting from the closed state without ligands, Simulation #C_3. (a) The evolution of the four variables during the simulation: RMSD reference to open (black curve) and closed (red curve) conformation, Angle of LID-CORE θ_1, Angle of NMP-CORE θ_2 and the distance between LID and NMP d_{LN}. The arrows highlight the events of conformational transitions. (b) Snapshots of the conformational changes during the simulation.

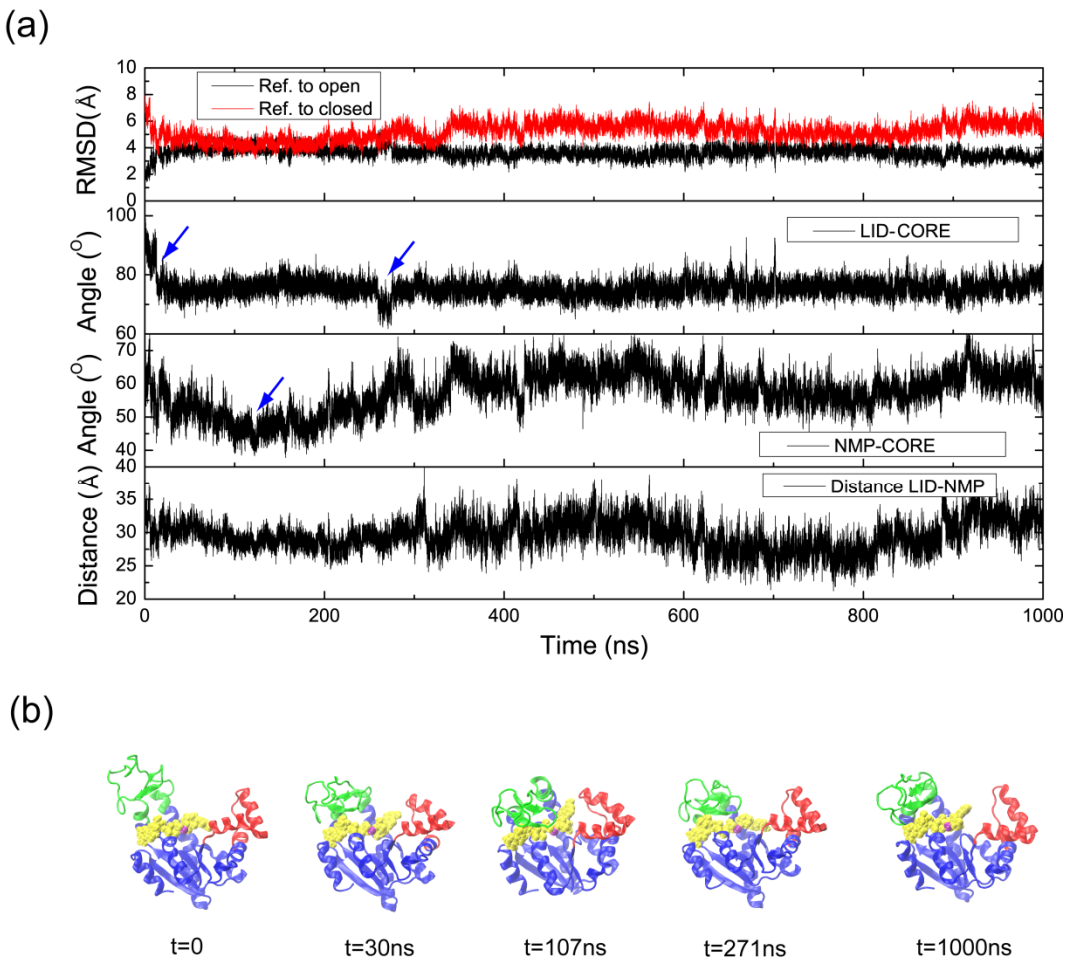

Figure S7. Conformational evolution of AdK starting from the open state with ligands ATP and AMP, simulation #O-ATP-AMP. (a) The evolution of the four variables during the simulation: RMSD reference to open (black curve) and closed (red curve) conformation, Angle of LID-CORE θ_1, Angle of NMP-CORE θ_2 and the distance between LID and NMP d_{LN}. The arrows highlight the events of conformational transitions. (b) Snapshots of the conformational changes during the simulation.

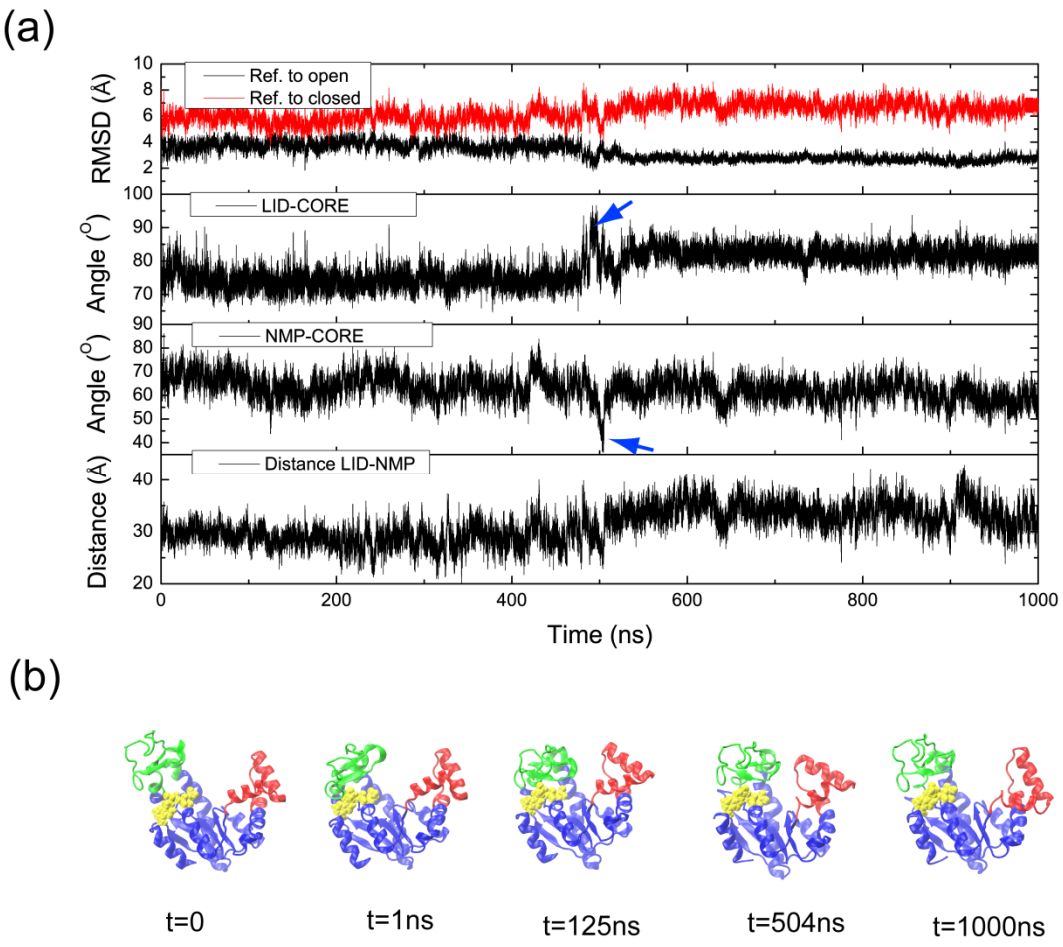

Figure S8. Conformational evolution of AdK starting from the open state with ATP only, simulation #O-ATP. (a) The evolution of the four variables during the simulation: RMSD reference to open (black curve) and closed (red curve) conformation, Angle of LID-CORE θ_1, Angle of NMP-CORE θ_2 and the distance between LID and NMP d_{LN}. The arrows highlight the events of conformational transitions. (b) Snapshots of the conformational changes during the simulation.

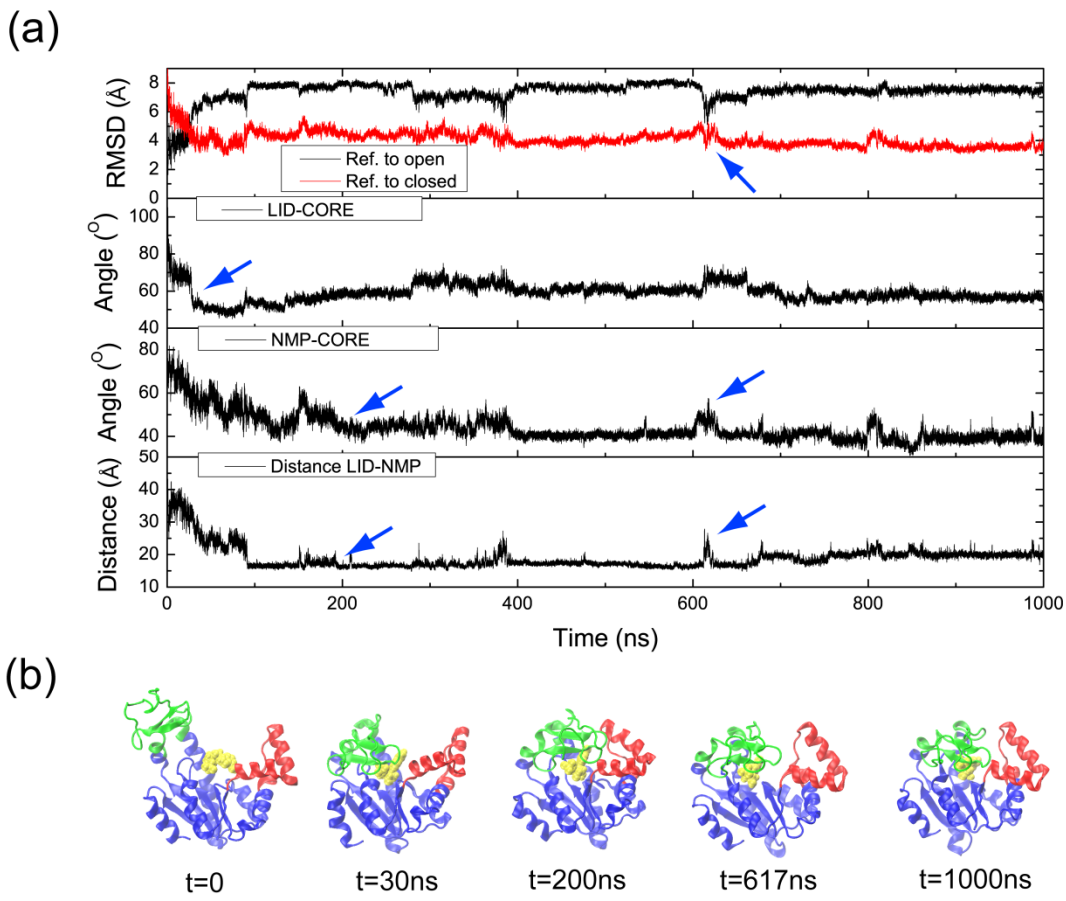

Figure S9. Conformational evolution of AdK starting from the open state with AMP only, simulation #O-AMP. (a) The evolution of the four variables during the simulation: RMSD reference to open (black curve) and closed (red curve) conformation, Angle of LID-CORE θ_1, Angle of NMP-CORE θ_2 and the distance between LID and NMP d_{LN}. The arrows highlight the events of conformational transitions. (b) Snapshots of the conformational changes during the simulation.

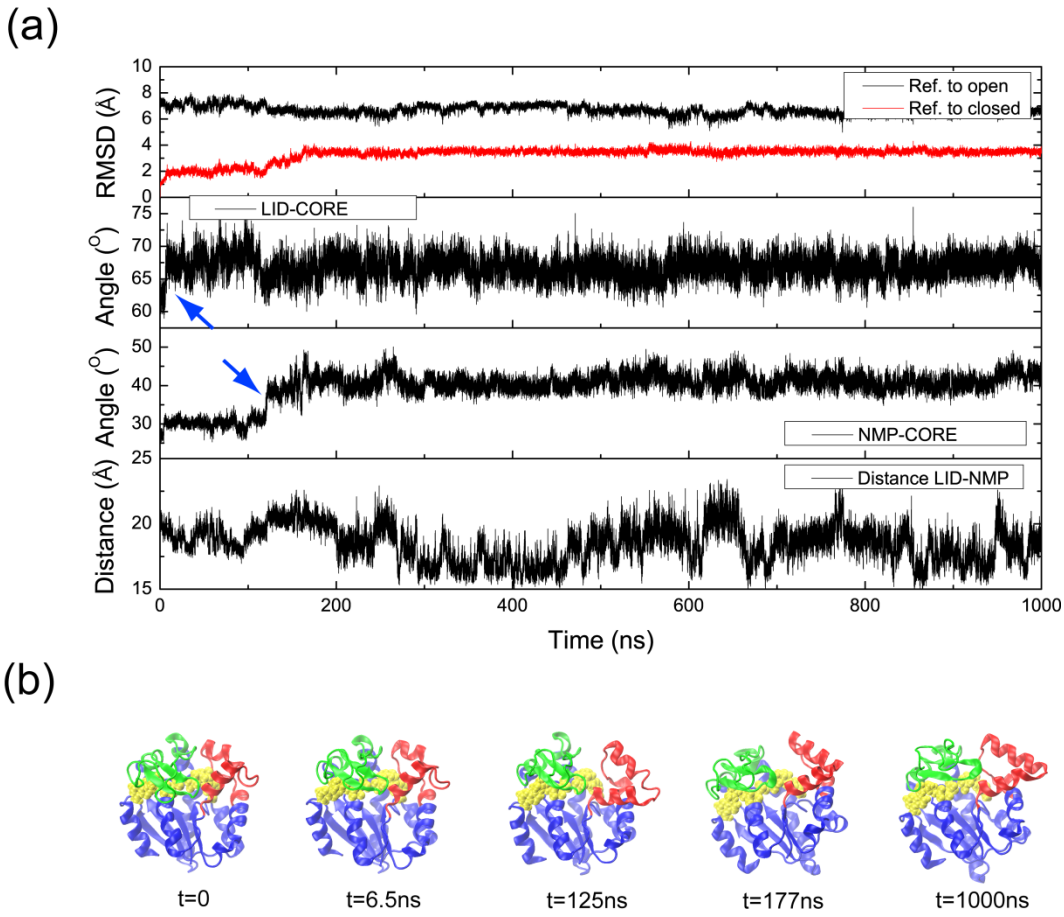

Figure S10. Conformational evolution of AdK starting from the closed state with ligand ATP and AMP, simulation #C-ATP-AMP. (a) The evolution of the four variables during the simulation: RMSD reference to open (black curve) and closed (red curve) conformation, Angle of LID-CORE θ_1, Angle of NMP-CORE θ_2 and the distance between LID and NMP d_{LN}. The arrows highlight the events of conformational transitions. (b) Snapshots of the conformational changes during the simulation.

(a)

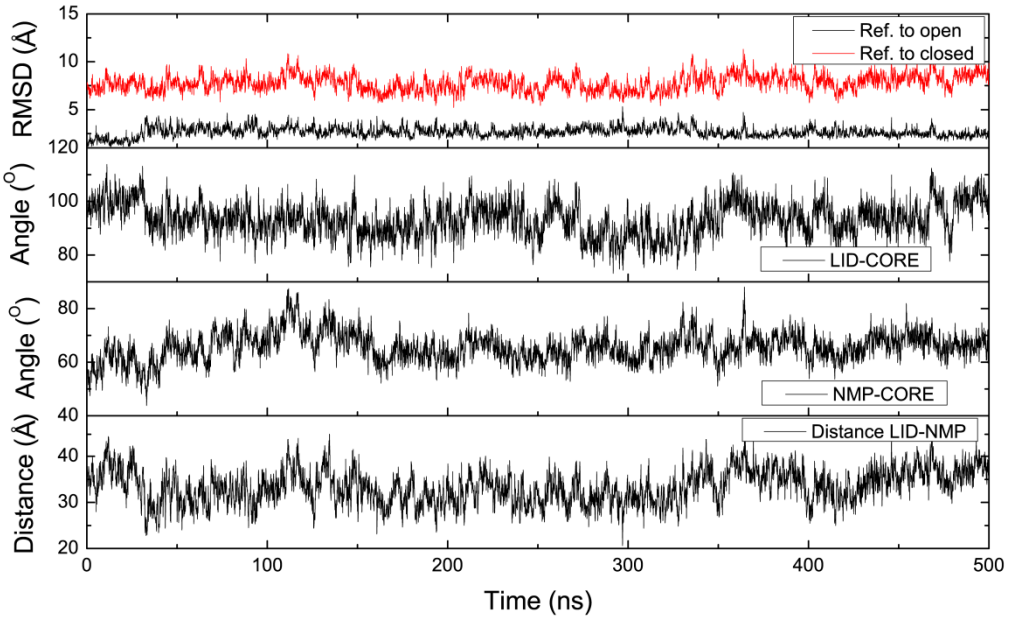

(b)

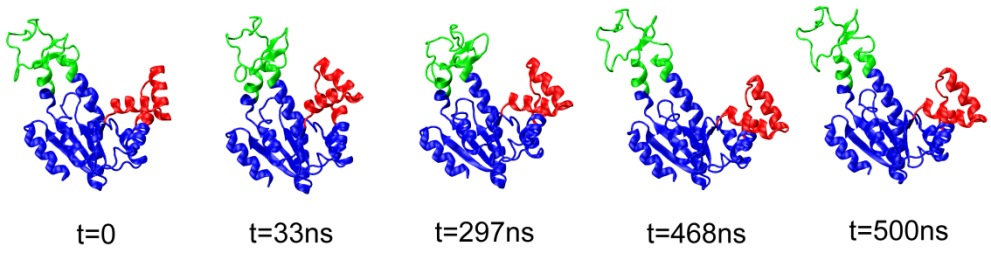

Figure S11. A 500ns MD simulation of conformational evolution of AdK starting from the open state without ligands, while using CHARMM27 force field with CMAP (33, 34). (a) The evolution of the four variables during the simulation: RMSD reference to the open (black curve) and the closed (red curve) conformation, Angle of LID-CORE θ_1, Angle of NMP-CORE θ_2 and the distance between LID and NMP d_{LN}. (b) Snapshots of the conformational states during simulation.

(a)

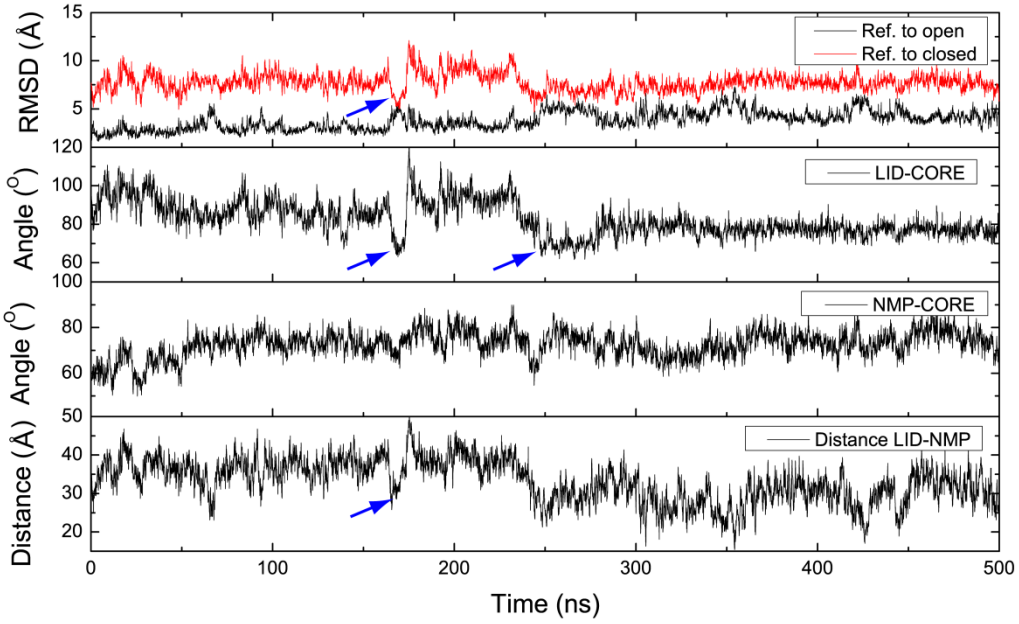

(b)

Figure S12. A 500ns MD simulation of conformational evolution of AdK starting from the open state without ligands, while using OPLS-AA force field (35, 36). (a) The evolution of the four variables during the simulation: RMSD reference to open (black curve) and closed (red curve) conformation, Angle of LID-CORE θ_1, Angle of NMP-CORE θ_2 and the distance between LID and NMP d_{LN}.The arrows highlight the events of conformational transitions. (b) Snapshots of the conformational states during simulation.

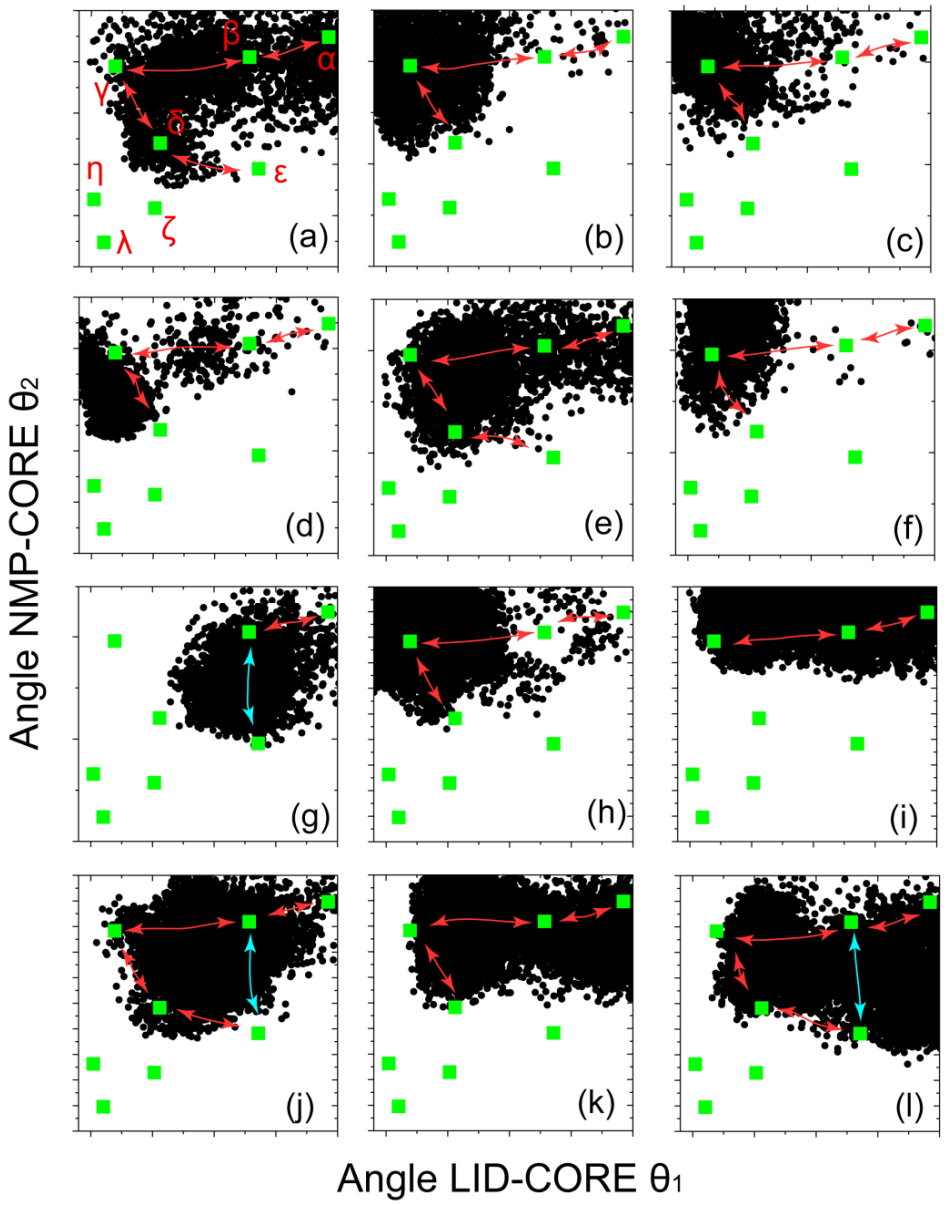

Figure S13. Transition pathways as revealed in the additional twelve 300ns timescale MD simulations (starting from the open state). The black dots are the angles θ_1 and θ_2 sampled in MD simulations. The green square symbols are the intermediate states as determined by Bias-exchange metadynamics simulations. The red arrows show the pathway that LID closes first and then NMP closes afterward, sampled by the MD simulations, while the cyan arrows show the pathways that NMP closes without the closure of LID domain. For clarity, the names of intermediate states are shown only in box (a).

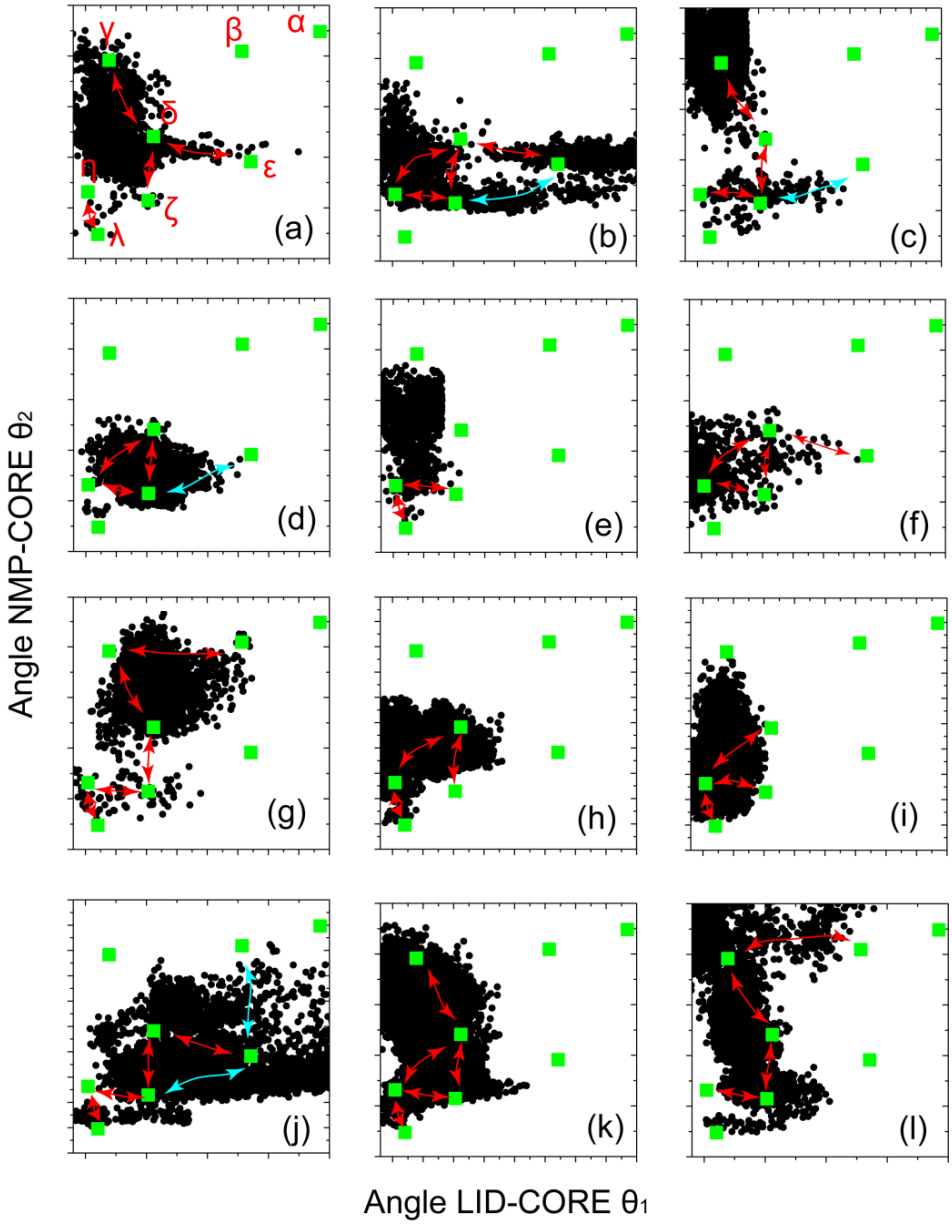

Figure S14. Transitional pathways as revealed in the additional twelve 300ns timescale MD simulations (starting from the closed state). The black dots are the angles θ_1 and θ_2 sampled in MD simulations. The green square symbols are the intermediate states as determined by Bias-exchange metadynamics simulations. The red arrows show the pathway that NMP opens first and then LID opens afterward, as sampled by the LT-MD simulations, while the cyan arrows show the pathways LID may open ahead of the opening of NMP domain. For clarity, the names of intermediate states are shown only in box (a).

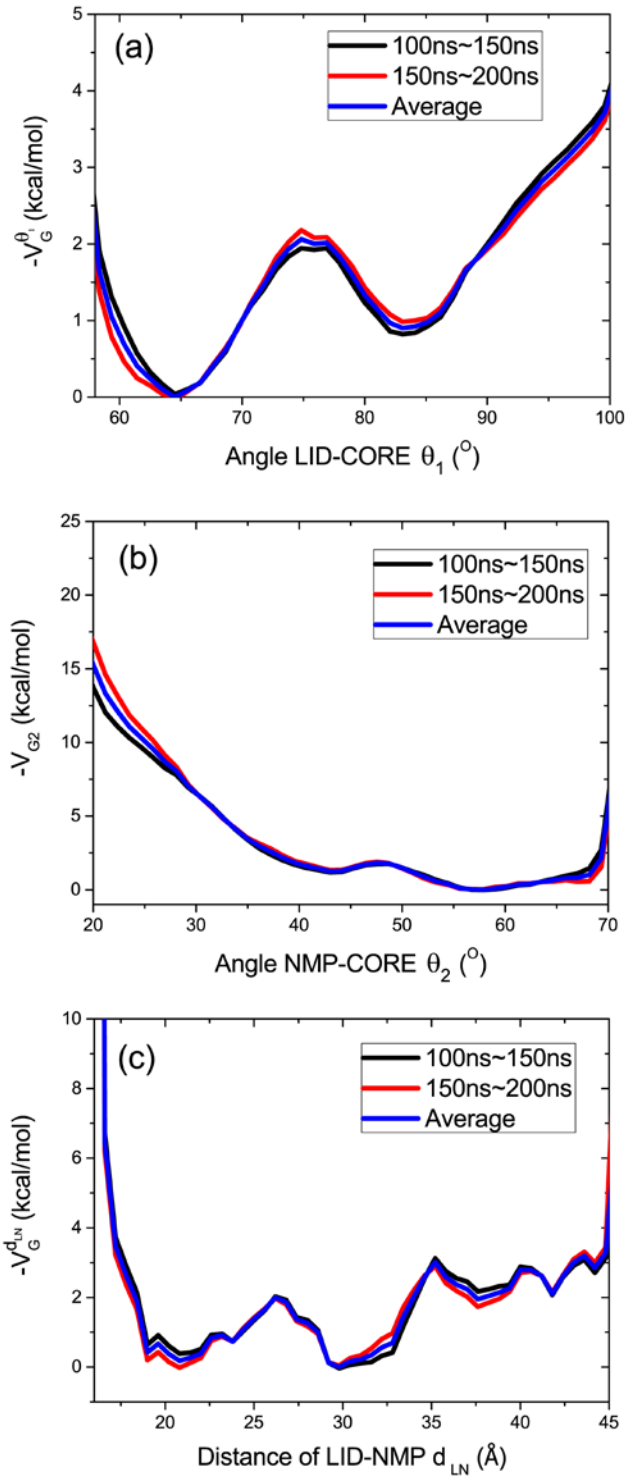

Figure S15. Convergence of bias profiles $V_G^i(S,t)$ without ligands.

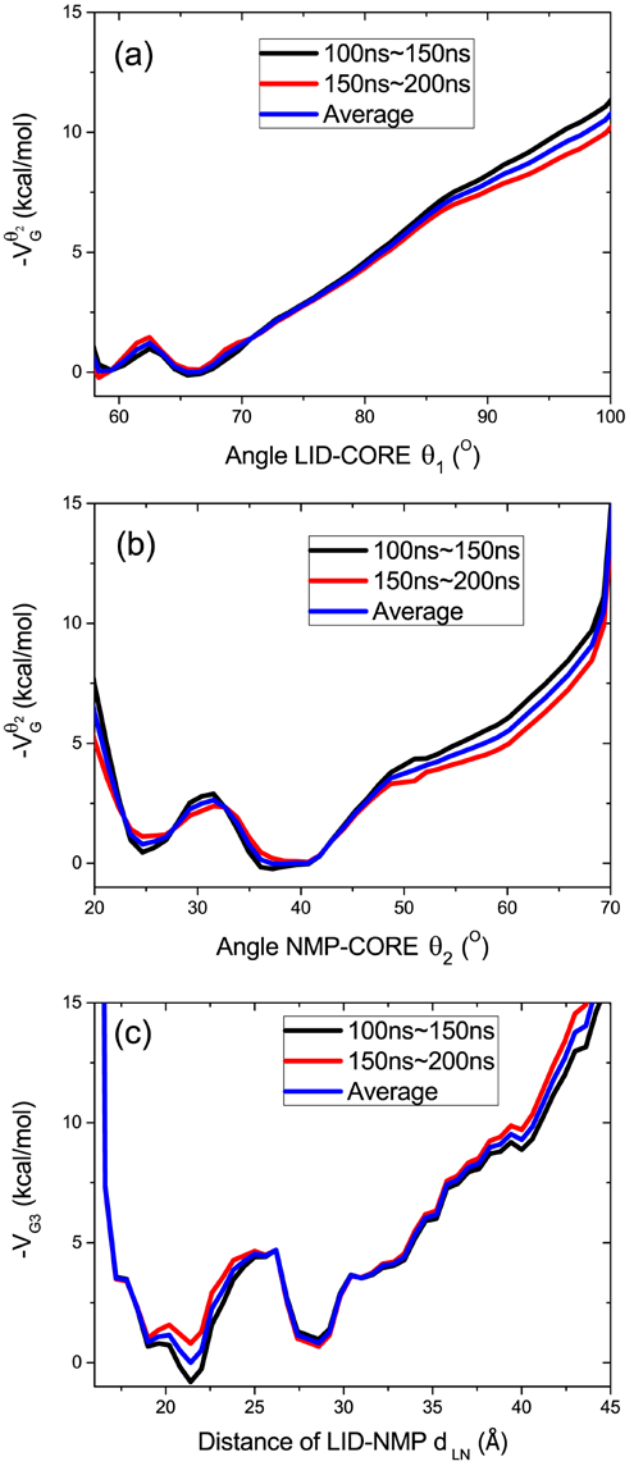

Figure S16. Convergence of bias profiles $V_G^i(S,t)$ with ligands.

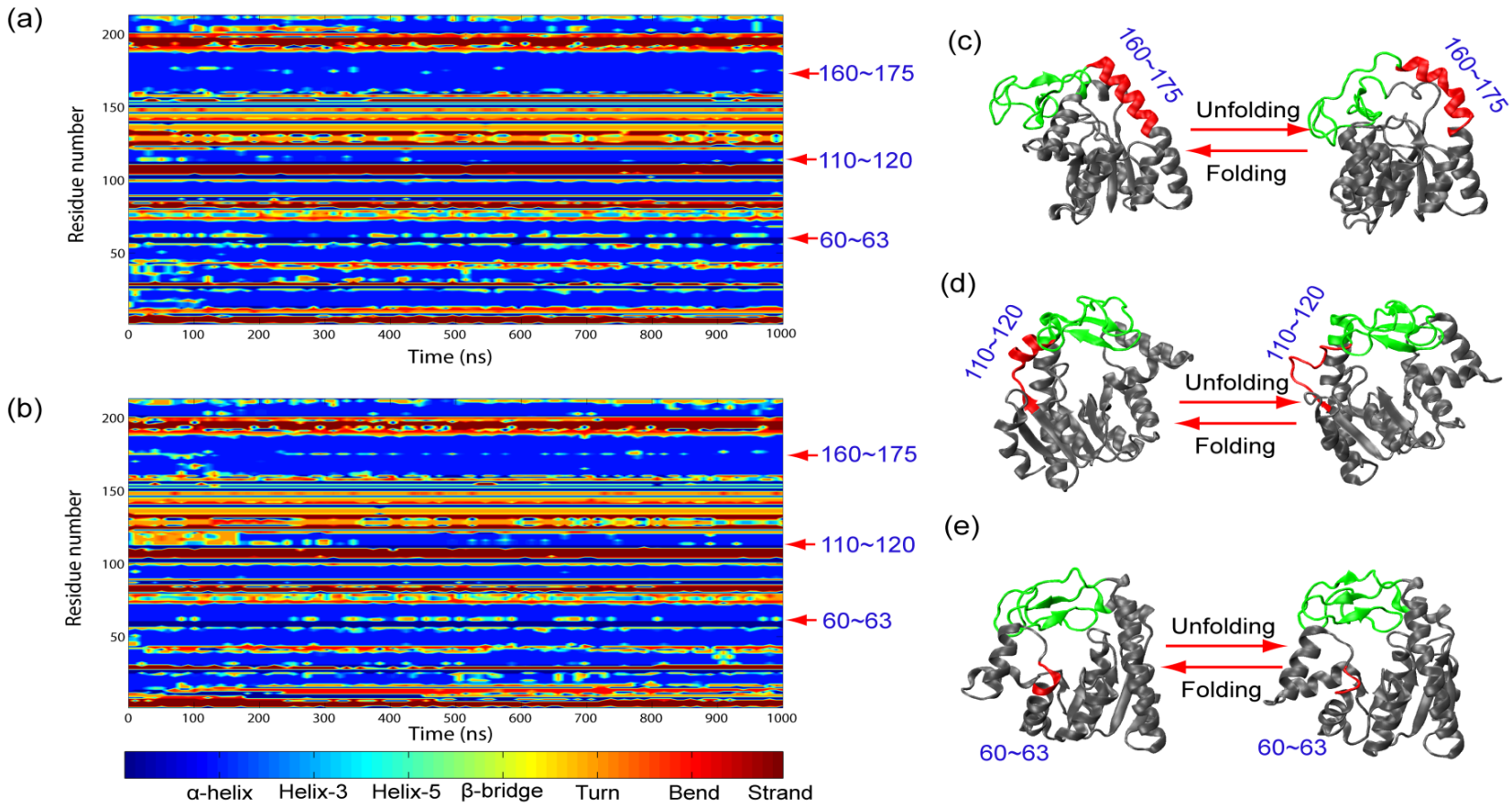

Figure S17. Structural spectrum of the AdK as a function of time for (a) Simulation # O1 starting from the open state and (b) simulation # C1 starting from the closed state, respectively. Typical regions of dynamics cracking: (c) Residues 60 to 63, (d) Residues 110 to 120 and (e) Residues 160 to 175, respectively. The color bar indicates the structural characters. The arrows in (a) and (b) indicate the regions for dynamics cracking. The color of the residue switches indicates the transition of the secondary structure, i.e. the local unfolding and folding cracking. The secondary structure of AdK is identified by DSSP package (37).

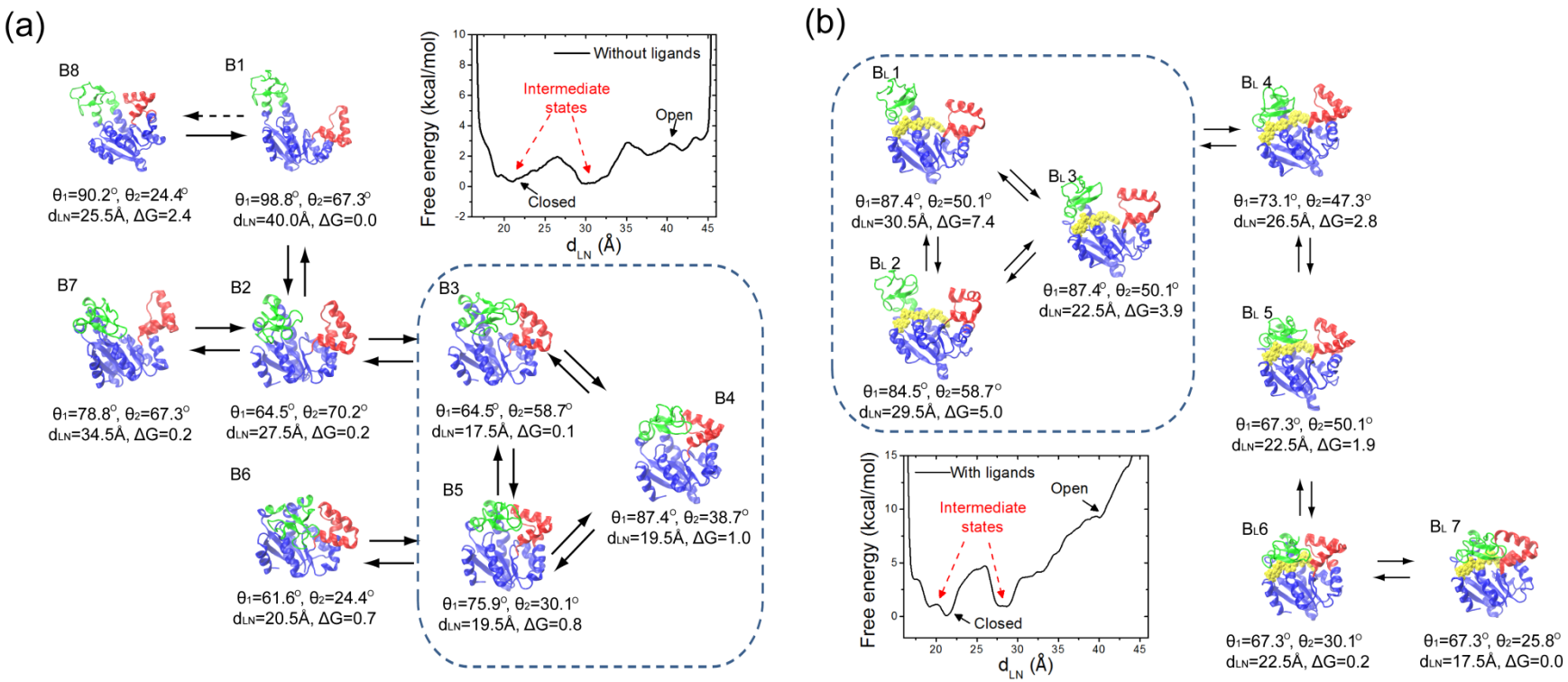

Figure S18. Conformational transitions and pathways of AdK (a) without ligands and (b) with ligands, respectively, as characterized by three CVs: $\boldsymbol{\theta_1}$, $\boldsymbol{\theta_2}$ and $\boldsymbol{d_{LN}}$. The inset curves show the one-dimensional free energy landscape if only against $\boldsymbol{d_{LN}}$. The reaction coordinates and the (relative) free energy of each state are printed out below the corresponding structure. The states B1 and B6 in (a) and B_L1 and B_L6 in (b) correspond to the crystal open and closed conformations, respectively, while the others are the intermediate states (e.g. semi-open-semi-closed like) conformations. The unit of the free energy is kcal/mol (1.0 kcal/mol equal to 1.7 k_BT at T = 300K).

Supporting reference:

1. Marinelli, F., F. Pietrucci, A. Laio, and S. Piana. 2009. A Kinetic Model of Trp-Cage Folding from Multiple Biased Molecular Dynamics Simulations. Plos Computational Biology 5.

2. Piana, S., and A. Laio. 2007. A bias-exchange approach to protein folding. Journal of Physical Chemistry B 111:4553-4559.

3. Pietrucci, F., F. Marinelli, P. Carloni, and A. Laio. 2009. Substrate Binding Mechanism of HIV-1 Protease from Explicit-Solvent Atomistic Simulations. Journal of the American Chemical Society 131:11811-11818.

4. Laio, A., and F. L. Gervasio. 2008. Metadynamics: a method to simulate rare events and reconstruct the free energy in biophysics, chemistry and material science. Reports on Progress in Physics 71:126601.

5. Laio, A., and M. Parrinello. 2002. Escaping free-energy minima. Proceedings of the National Academy of Sciences 99:12562-12566.

6. Barducci, A., G. Bussi, and M. Parrinello. 2008. Well-tempered metadynamics: A smoothly converging and tunable free-energy method. Physical Review Letters 100:020603.

7. Berendsen, H. J. C., D. Vanderspoel, and R. Vandrunen. 1995. Gromacs - a Message-Passing Parallel Molecular-Dynamics Implementation. Computer Physics Communications 91:43-56.

8. Lindahl, E., B. Hess, and D. van der Spoel. 2001. GROMACS 3.0: a package for molecular simulation and trajectory analysis. Journal of Molecular Modeling 7:306-317.

9. Bonomi, M., D. Branduardi, G. Bussi, C. Camilloni, D. Provasi, P. Raiteri, D. Donadio, F. Marinelli, F. Pietrucci, and R. A. Broglia. 2009. PLUMED: A portable plugin for free-energy calculations with molecular dynamics. Computer Physics Communications 180:1961-1972.

10. Biarnés, X., F. Pietrucci, F. Marinelli, and A. Laio. 2012. METAGUI. A VMD interface for analyzing metadynamics and molecular dynamics simulations. Computer Physics Communications 183:203-211.

11. Humphrey, W., A. Dalke, and K. Schulten. 1996. VMD: Visual molecular dynamics. J Mol Graph 14:33-38.

12. Hänggi, P., P. Talkner, and M. Borkovec. 1990. Reaction-rate theory: fifty years after Kramers. Rev. Mod. Phys. 62:251.

13. Sriraman, S., I. G. Kevrekidis, and G. Hummer. 2005. Coarse master equation from Bayesian analysis of replica molecular dynamics simulations. The Journal of Physical Chemistry B 109:6479-6484.

14. Hummer, G. 2005. Position-dependent diffusion coefficients and free energies from Bayesian analysis of equilibrium and replica molecular dynamics simulations. New Journal of Physics 7:34.

15. Muller, C. W., G. J. Schlauderer, J. Reinstein, and G. E. Schulz. 1996. Adenylate kinase motions during catalysis: An energetic counterweight balancing substrate binding. Structure 4:147-156.

16. Henzler-Wildman, K. A., V. Thai, M. Lei, M. Ott, M. Wolf-Watz, T. Fenn, E. Pozharski, M. A. Wilson, G. A. Petsko, M. Karplus, C. G. Huebner, and D. Kern. 2007. Intrinsic motions along an enzymatic reaction trajectory. Nature 450:838-U813.

17. Dreusicke, D., P. A. Karplus, and G. E. Schulz. 1988. Refined structure of porcine cytosolic adenylate kinase at 2.1 Å resolution. Journal of Molecular Biology 199:359-371.

18. Mukhopadhyay, A., A. Kladova, S. Bursakov, O. Y. Gavel, J. Calvete, V. Shnyrov, I. Moura, J. Moura,

M. Romão, and J. Trincão. 2011. Crystal structure of the zinc-, cobalt-, and iron-containing adenylate kinase from Desulfovibrio gigas: a novel metal-containing adenylate kinase from Gram-negative bacteria. JBIC Journal of Biological Inorganic Chemistry 16:51-61.

19. Schlauderer, G., and G. Schulz. 1996. The structure of bovine mitochondrial adenylate kinase: comparison with isoenzymes in other compartments. Protein Science 5:434-441.

20. Muller, C. W., and G. E. Schulz. 1992. STRUCTURE OF THE COMPLEX BETWEEN ADENYLATE KINASE FROM ESCHERICHIA-COLI AND THE INHIBITOR AP5A REFINED AT 1.9 A RESOLUTION - A MODEL FOR A CATALYTIC TRANSITION-STATE. Journal of Molecular Biology 224:159-177.

21. Müller, C. W., and G. E. Schulz. 1993. Crystal structures of two mutants of adenylate kinase from Escherichia coli that modify the Gly‐loop. Proteins: Structure, Function, and Bioinformatics 15:42-49.

22. Schrank, T. P., D. W. Bolen, and V. J. Hilser. 2009. Rational modulation of conformational fluctuations in adenylate kinase reveals a local unfolding mechanism for allostery and functional adaptation in proteins. Proceedings of the National Academy of Sciences 106:16984-16989.

23. Berry, M. B., E. Y. Bae, T. R. Bilderback, M. Glaser, and G. N. Phillips. 2006. Crystal structure of ADP/AMP complex of Escherichia coli adenylate kinase. Proteins-Structure Function and Bioinformatics 62:555-556.

24. Berry, M. B., B. Meador, T. Bilderback, P. Liang, M. Glaser, and G. N. Phillips. 1994. THE CLOSED CONFORMATION OF A HIGHLY FLEXIBLE PROTEIN - THE STRUCTURE OF ESCHERICHIA-COLI ADENYLATE KINASE WITH BOUND AMP AND AMPPNP. Proteins-Structure Function and Genetics 19:183-198.

25. Bae, E., and G. N. Phillips. 2004. Structures and analysis of highly homologous psychrophilic, mesophilic, and thermophilic adenylate kinases. Journal of Biological Chemistry 279:28202-28208.

26. Couñago, R., S. Chen, and Y. Shamoo. 2006. In vivo molecular evolution reveals biophysical origins of organismal fitness. Molecular cell 22:441-449.

27. Abele, U., and G. Schulz. 1995. High‐resolution structures of adenylate kinase from yeast ligated with inhibitor Ap5A, showing the pathway of phosphoryl transfer. Protein Science 4:1262-1271.

28. Spuergin, P., U. Abele, and G. E. Schulz. 1995. Stability, activity and structure of adenylate kinase mutants. European Journal of Biochemistry 231:405-413.

29. Schlauderer, G., K. Proba, and G. Schulz. 1996. Structure of a mutant adenylate kinase ligated with an ATP-analogue showing domain closure over ATP. Journal of Molecular Biology 256:223-227.

30. Wild, K., R. Grafmüller, E. Wagner, and G. E. Schulz. 1997. Structure, catalysis and supramolecular assembly of adenylate kinase from maize. European Journal of Biochemistry 250:326-331.

31. Davlieva, M., and Y. Shamoo. 2009. Structure and biochemical characterization of an adenylate kinase originating from the psychrophilic organism Marinibacillus marinus. Acta Crystallographica Section F: Structural Biology and Crystallization Communications 65:751-756.

32. Berry, M. B., and G. N. Phillips Jr. 1998. Crystal structures of Bacillus stearothermophilus adenylate kinase with bound Ap5A, Mg2 Ap5A, and Mn2 Ap5A reveal an intermediate lid position and six coordinate octahedral geometry for bound Mg2 and Mn2. Proteins 32:276-288.

33. MacKerell, A. D., D. Bashford, M. Bellott, R. L. Dunbrack, J. D. Evanseck, M. J. Field, S. Fischer, J. Gao, H. Guo, S. Ha, D. Joseph-McCarthy, L. Kuchnir, K. Kuczera, F. T. K. Lau, C. Mattos, S.

Michnick, T. Ngo, D. T. Nguyen, B. Prodhom, W. E. Reiher, B. Roux, M. Schlenkrich, J. C. Smith, R. Stote, J. Straub, M. Watanabe, J. Wiorkiewicz-Kuczera, D. Yin, and M. Karplus. 1998. All-atom empirical potential for molecular modeling and dynamics studies of proteins. Journal of Physical Chemistry B 102:3586-3616.

34. MacKerell, A. D., M. Feig, and C. L. Brooks. 2004. Improved treatment of the protein backbone in empirical force fields. Journal of the American Chemical Society 126:698-699.

35. Kaminski, G. A., R. A. Friesner, J. Tirado-Rives, and W. L. Jorgensen. 2001. Evaluation and reparametrization of the OPLS-AA force field for proteins via comparison with accurate quantum chemical calculations on peptides. The Journal of Physical Chemistry B 105:6474-6487.

36. Jorgensen, W. L., D. S. Maxwell, and J. Tirado-Rives. 1996. Development and testing of the OPLS all-atom force field on conformational energetics and properties of organic liquids. Journal of the American Chemical Society 118:11225-11236.

37. Kabsch, W., and C. Sander. 1983. DICTIONARY OF PROTEIN SECONDARY STRUCTURE - PATTERN-RECOGNITION OF HYDROGEN-BONDED AND GEOMETRICAL FEATURES. Biopolymers 22:2577-2637.